Icarus 201 (2009) 198–216

Contents lists available at ScienceDirect

Icarus

www.elsevier.com/locate/icarus

Titan solar occultation observed by *Cassini*/VIMS: Gas absorption and constraints on aerosol composition

A. Bellucci [a], B. Sicardy [a,b,*], P. Drossart [a], P. Rannou [c,d], P.D. Nicholson [e], M. Hedman [e], K.H. Baines [f], B. Burrati [f]

[a] *Laboratoire d'Etudes Spatiales (LESIA), Observatoire de Paris, Univserité Pierre et Marie Curie, Université Paris-Diderot, 5 Place Jules Janssen, 92195 Meudon, France*
[b] *Institut Universitaire de France, 103, bd Saint-Michel, 75005 Paris, France*
[c] *GSMA (UMR 6089) Université de Reims Champagne-Ardenne, 51687 Reims cedex, France*
[d] *Service d'Aéronomie (UMR 7620) Université de Versailles St. Quentin, 91370 Verrières le Buisson, France*
[e] *Cornell University, Department of Astronomy, Space Science Bldg., Ithaca, NY 14853, USA*
[f] *Jet Propulsion Laboratory, 4800 Oak Grove Drive, Pasadena, CA 91109, USA*

ARTICLE INFO

Article history:
Received 5 June 2008
Revised 21 November 2008
Accepted 12 December 2008
Available online 31 December 2008

Keywords:
Titan
Occultations
Atmospheres, composition

ABSTRACT

A solar occultation by Titan's atmosphere has been observed through the solar port of the *Cassini*/VIMS instrument on January 15th, 2006. Transmission spectra acquired during solar egress probe the atmosphere in the altitude range 70 to 900 km at the latitude of 71° S. Several molecular absorption bands of CH_4 and CO are visible in these data. A line-by-line radiative transfer calculation in spherical geometry is used to model three methane bands (1.7, 2.3, 3.3 μm) and the CO 4.7 μm band. Above 200 km, the methane 2.3 μm band is well fit with constant mixing ratio between 1.4 and 1.7%, in agreement with *in situ* and other *Cassini* measurements. Under 200 km, there are discrepancies between models and observations that are yet fully understood. Under 480 km, the 3.3 μm CH_4 band is mixed with a large and deep additional absorption. It corresponds to the C–H stretching mode of aliphatic hydrocarbon chains attached to large organic molecules. The CO 4.7 μm band is observed in the lower stratosphere (altitudes below 150 km) and is well fit with a model with constant mixing ratio of 33 ± 10 ppm. The continuum level of the observed transmission spectra provides new constraints on the aerosol content of the atmosphere. A model using fractal aggregates and optical properties of tholins produced by Khare et al. [Khare, B.N., Sagan, C., Arakawa, E.T., Suits, F., Callcott, T.A., Williams, M.W., 1984. Icarus 60, 127–137] is developed. Fractal aggregates with more than 1000 spheres of radius 0.05 μm are needed to fit the data. Clear differences in the chemical composition are revealed between tholins and actual haze particles. Extinction and density profiles are also retrieved using an inversion of the continuum values. An exponential increase of the haze number density is observed under 420 km with a typical scale height of 60 km.

1. Introduction

Titan's atmosphere has been studied for a long time through ground-based observations and more recently from space. Since 2004, the *Cassini/Huygens* mission has provided new insights on that atmosphere through combined *in situ* and remote sensing observations. The complex chemistry in this environment leads to the formation of haze particles that are responsible for the orange color of Titan. The methane rich atmosphere exhibits several absorption bands in the near infrared, making the surface visible only in narrow spectral windows. The study of Titan's atmosphere from the *Cassini* orbiter and *Huygens* probe has provided a large amount of data on the composition of gases and aerosols. The atmospheric composition in the upper atmosphere has been studied by the Composite Infrared Spectrometer (CIRS) in the far infrared (Coustenis et al., 2007; de Kok et al., 2007), while the VIMS instrument (Visible and Infrared Mapping Spectrometer) has provided information in the near infrared (Griffith et al., 2006; Baines et al., 2005, 2006). *Huygens* observations have provided temperature profiles as well as aerosol distribution (Fulchignoni et al., 2005; Tomasko et al., 2008). Nevertheless, constraints on the composition of the haze are still elusive. New dedicated observations of aerosols are therefore welcome to enhance our knowledge of the Titan's atmosphere.

This paper presents observations of Titan taken by the *Cassini*/VIMS instrument in the solar occultation mode, which allow us to sound the atmosphere of Titan over a large altitude range. The second section of this paper describes the instrument and observations, while data reduction is presented in the third section,

* Corresponding author at: Laboratoire d'Etudes Spatiales (LESIA), Observatoire de Paris, Univserité Pierre et Marie Curie, Université Paris-Diderot, 5 Place Jules Janssen, 92195 Meudon, France.
E-mail address: bruno.sicardy@obspm.fr (B. Sicardy).

0019-1035/$ – see front matter
doi:10.1016/j.icarus.2008.12.024

before modeling and interpretation of molecular absorption (Section 5). The fifth part deals with the aerosol content of the atmosphere.

2. Presentation of the instrument and observations

The VIMS instrument is an imaging spectrometer that spans visual and infrared wavelength from 0.3 to 5.1 μm (cf. Brown et al., 2004). For Titan, this instrument has been mainly used for limb observations to study the atmosphere, particularly atmospheric emissions (Baines et al., 2006) and nadir detection of the surface in the so-called CH_4 windows where the atmosphere is less opaque. By contrast, this paper presents data obtained in a VIMS occultation mode. Stellar occultations have proved in the past to be a powerful tool to probe planetary atmospheres. For Earth-based observations, differential refraction of stellar rays in the planet's atmosphere is usually the dominating factor that shapes the lightcurves. Inversion methods then provide a density profile at typical pressure levels of a fraction of mbar to a fraction of μbar. In the case of ground-based stellar occultations by Titan, some information can be gathered on the distribution and properties of the haze, as well as the zonal wind regime if the central flash is detected (see Sicardy et al., 2006, and references therein for details). With the *Cassini* spacecraft, it is possible to observe occultations of the Sun or bright stars by Titan's atmosphere, while being very close to the satellite. The deepest levels probed by refracted rays have densities that vary roughly as $1/D$, where D is the distance of the observer to Titan. Consequently, close observations by a spacecraft probe denser, thus deeper, altitude levels than Earth-based observations. This is illustrated in Fig. 1, where the levels corresponding to 1 and 50% *refractive* attenuation are shown as a function of distance D to Titan. During the solar occultation presented here, the *Cassini* spacecraft was at a distance between 8000 and 10,000 km from Titan's center. For this range of D, the refractive 50% (resp. 1%) attenuation occurs below 100 km (resp. 150 km). However, we will see that in the actual VIMS occultation lightcurves, the drop occurs at much higher altitudes because of absorption by gases or hazes.

Here we report about the first solar occultation by Titan observed with the VIMS instrument.

On January 15th, 2006, during Cassini's 10th flyby of Titan (T10), the VIMS instrument observed the ingress and egress of the Sun through Titan's atmosphere. Ingress occurred at a latitude of about 41° S and egress near 71° S. Because of the brightness of the Sun, the observations are not done through the main aperture of the instrument. A special "solar port" was designed for observations of solar occultations. This port is offset from the boresight direction by 20° and is aligned with the UVIS solar occultation port. Its goal is to attenuate the solar flux, which is achieved through a series of reflections inside the solar port. The light beam that exits the solar port is then focused by the telescope optics into the VIMS-IR entrance slit, and subsequently follows the same path in the IR spectrometer as the beam that directly enters the main port. Ground calibration has shown that the attenuation factor is about 2.5×10^{-7}. Some sunlight is scattered within the optics of the solar port. This induces some stray light around the image of the Sun. As a consequence, the background level is different from zero even when we observe far from Titan. We checked that this signal has the same spectrum as the Sun, and concluded that these solar photons should not be removed from the signal. We also note that the image of the Sun is elongated and not circular as it was reported during the calibration process (Brown et al., 2004).

During this observation, only the 256 infrared spectral channels where used, covering the interval 0.85 to 5.1 μm with a spectral resolution of 16 nm. The standard IMAGE operating mode was used with 12×12 spatial pixels at an angular resolution of 0.5×0.5 mrad per pixel, and an exposure time of 40 ms. The acquisition time of each cube is 6.9 s. With a total field of view (FOV) of 6×6 mrad and a distance of observation between 8000 and 10,000 km, each image covers a typical portion of atmosphere of 50 to 60 km in size in each direction. The size of the solar disk in the atmosphere perpendicular to the line of sight is about 7 to 10 km (depending of the distance of VIMS to Titan). This size is smaller than the typical scale height (about 40 km), therefore does not affect our analysis. In total, 617 cubes were acquired during the observations. Among them, 63 cubes cover the Sun egress and are studied more specifically here (cubes V1516019443_1.QUB to V1516019894_1.QUB). The other ones are eliminated (in particular, the ingress cubes, see below) or used to compute a reference solar spectrum. Thus VIMS data cubes of this observation can be analyzed in two ways: Each of the 256 spectral channels provides an occultation lightcurve. Conversely, the 63 cubes of interest provide 63 spectra of the Sun observed through different levels of Titan's atmosphere.

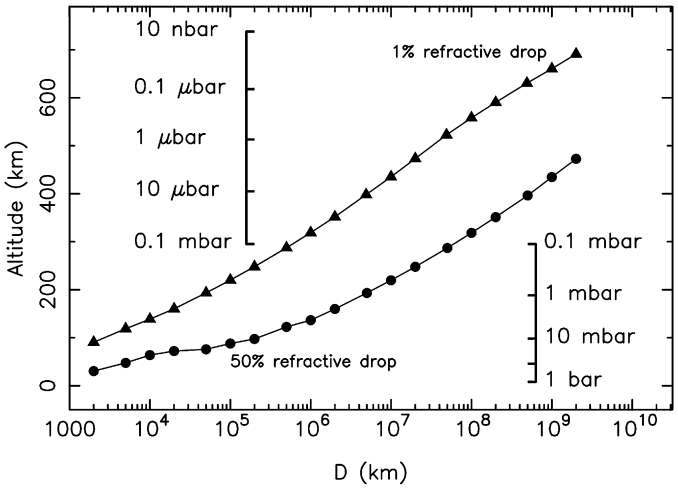

Fig. 1. Assuming a transparent atmosphere, altitudes corresponding to the 1% (triangles) and 50% (dots) drops in a refractive ligthcurve are plotted against the distance D of the observer to Titan. Corresponding pressure levels are also represented. This figure was obtained using a ray tracing program and an atmospheric model from Yelle et al. (1991).

During this observation, thrusters were used for the stabilization of the spacecraft. This stabilization method is less stable that the reaction wheels usually used but it is necessary when the spacecraft is close to Titan where the drag due to the extended atmosphere is relatively high. The limited torque provided by the wheels must be larger than the atmospheric drag not to loose the attitude control of the spacecraft. This was not possible during this flyby. Consequently, the Sun did not stay fully inside the VIMS field of view (FOV) during ingress and part of the solar flux is missing, rendering ingress data unusable. During egress, the Sun stayed inside the VIMS FOV but still moved inside of it. This motion of the Sun in the VIMS may introduce small errors in the normalized spectra. Additional errors will be due to variations of the part of the scattered light included in the 12×12 pixels FOV, as the scattered light spectrum is not quite the same as the solar image spectrum.

3. Data reduction

3.1. Altitude retrieval

Each VIMS cube is spatially summed to provide one spectrum of the Sun observed through Titan's atmosphere. While the sunlight had to pass through the atmosphere at multiple altitudes, we define the level sounded by each cube as the deepest level probed

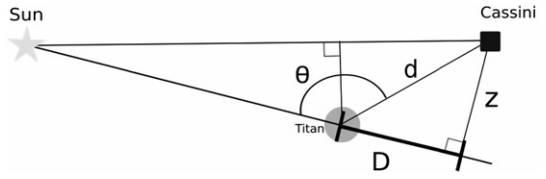

Fig. 2. Definition of the geometrical parameters used in the calculation of the altitudes probed by each cube. The phase angle θ and the distance d from *Cassini* to Titan's center are given by SPICE kernels. Distances D and z are retrieved by simple geometry. This figure does not represent the refraction effect, only the relative positions of the relevant objects.

by the light, as this level has the largest contribution to absorption and refraction effects. This minimum altitude is computed using navigation data and accounting for the refraction.

The relative positions of *Cassini* spacecraft, Titan and the Sun are computed using the NAIF/SPICE system. Relevant quantities are the solar phase angle, θ, and the distance d between the *Cassini* spacecraft and Titan's center (Fig. 2). We call Z the distance from *Cassini* to the Sun–Titan line ($Z = d\cos\theta$), and D the distance between Titan's center and the projection of *Cassini* on the Sun–Titan line ($D = d\sin\theta$). Note that Z corresponds to the position of the observer in the shadow in the case of an Earth-based observation. Thus, for each data cube, the position of *Cassini* relative to Titan is described by the pair (D, Z).

These values are entered in a ray-tracing program that calculates the differential refraction of a set of initially parallel light rays from the Sun (Sicardy et al., 2006). To model the atmosphere, a density profile from Yelle (1991) is used instead of the Huygens Atmospheric Structure Instrument (HASI) data (Fulchignoni et al., 2005), since the local inhomogeneities of this latter profile results in many spikes in the lightcurve. Note that we made this choice for refraction models only, while the HASI profile is used later in this paper for radiative transfer calculations. This choice does not affect much our result. In the ray tracing analysis, the atmosphere is assumed to be composed of 98% N_2 and 2% CH_4, but refraction depends only weakly on these values. The atmosphere is divided in 100 m-thick layers between 1300 km altitude and the surface. A ray coming from the Sun with an impact parameter r (the minimum distance of the ray to Titan center) is refracted by an angle $d\omega$ in each layer. For each position (D, Z), that is for each cube, the code provides the minimum altitude reached by the light rays and the flux $\phi(D, Z)$ that would be received with only refraction taken into account, i.e. assuming a transparent atmosphere. This calculation is done for each of the 256 wavelengths, as the refraction depends slightly on the wavelength. The 256 values of the minimum altitude are spectrally averaged to give z_0, the minimum altitude for the corresponding data cube. For the egress cubes, the vertical sampling is smaller than 20 km, smaller than the atmospheric scale height.

3.2. Lightcurves

For the data reduction, we proceed in two steps. First, we compute the lightcurves and make the appropriate corrections. This is presented in this subsection followed by a short analysis of the ligthcurves. Then, we produce transmission spectrum by normalizing the lightcurves. This is the subject of the next subsection.

The 617 data cubes were calibrated using the VIMS online calibration routine (McCord et al., 2004). The IR background was automatically subtracted, the current IR flatfield applied, and DN (Data Number) were multiplied by the instrument performance model, and finally converted into specific energy.

The 144 pixels of each cube in each band are summed, resulting in 256 lightcurves or 63 spectra obtained during egress. Some of the egress lightcurves are presented in Fig. 3. They show the solar flux as a function of the minimum altitude z_0 defined above. These initial lightcurves, $\Phi_{0,\lambda}(z_0)$, do not have a constant flux at high altitude: the solar flux appears to increase monotonically with altitude. We check on the VIMS navigation software (DETOUR) that no bright object was in the FOV of the main VIMS aperture. We do not expect any excess light when the instrument is pointing to the Sun at more than 1000 km above Titan's surface: only the solar flux is received at these altitudes. We do not expect any flux from Titan

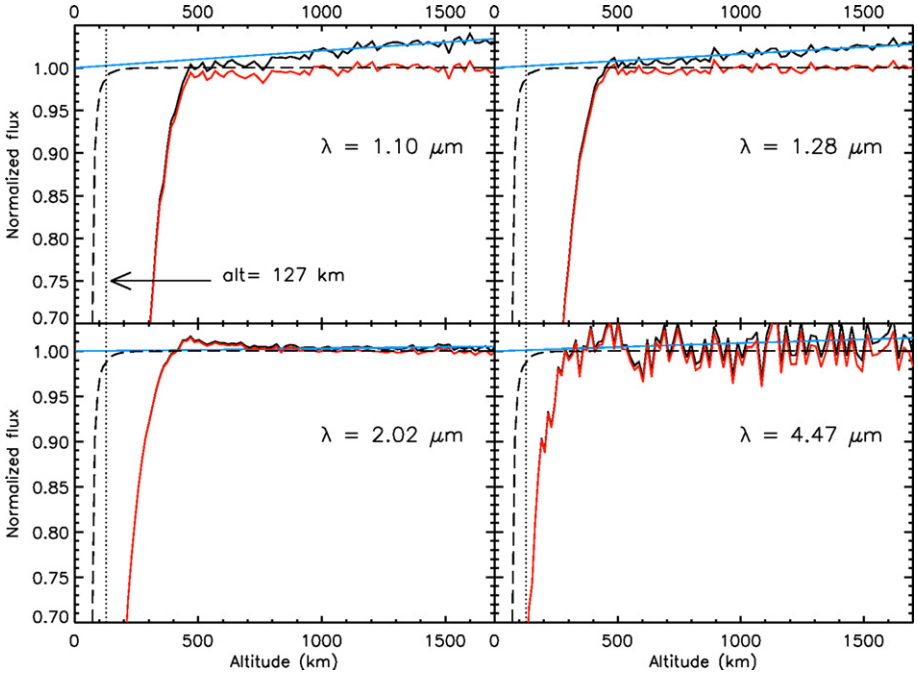

Fig. 3. VIMS observed lightcurves before correction are shown in black at four different wavelengths. The straight line used for correction is in blue. Both were normalized to unity as explained in text. The corrected and normalized lightcurves are in red. The dashed lines represent the theoretical lightcurves in a clear atmosphere (refraction only). When only differential refraction is present, we see a decrease (1% drop) of light for altitudes lower than 127 km (dotted vertical line). The observed lightcurves (red) begin to decrease at much higher altitudes because of gas and haze absorption. Note in the 2.02 μm lightcurve the increase of signal just below 500 km (see text).

because of the extremely large attenuation factor in the solar port. Thus we attribute these low frequency variations to some instrumental effects that are not yet fully understood. Perhaps they are due to the motion of the Sun in the field of view and the resulting changes in the scattered light intensity within the solar port.

For each wavelength, a linear fit in $a_\lambda z_0 + b_\lambda$ is performed on the lightcurve $\Phi_{0,\lambda}(z_0)$ between 1000 and 2000 km (this includes 49 points). These limits are chosen to be close enough to the occultation, so that the linear fit remains a reasonable assumption. We note that the slope decreases with increasing wavelength. In order to correct the flux variation outside the occultation, but not the mean level, the slope is corrected by dividing each lightcurve $\Phi_{0,\lambda}(z_0)$ by $\frac{a_\lambda}{b_\lambda} z_0 + 1$. The corrected lightcurves are presented in Fig. 3 (red curves). They were normalized (see below) in order to be compared to each other. For lightcurves taken around 2 μm (corresponding to a continuum wavelength in the spectra), we note an increase of the flux above unity for altitudes between 400 and 500 km (see for instance the lower left panel of Fig. 3). This altitude range corresponds to the clear area between the main layer and the detached haze (Porco et al., 2005). This effect could be due to forward scattering of the detached haze layer in the FOV while the Sun is shining in the clear zone. However we do not see this 'bump' at other wavelengths. One possibility is that it could be concealed by haze absorption at shorter wavelengths, and hidden in the noise at longer ones. We leave this potentially interesting feature for future work.

In the lightcurves presented in Fig. 3, we can see that the solar flux decreases at much higher altitude than expected from the purely refractive model with a transparent atmosphere. A 5% drop is reached at about 440 km at 1 μm, at about 340 km at 2 μm and at about 300 km at 4 μm. These observed drops are caused by *absorption* by gas and haze. Thus, the *Cassini* spacecraft observes occultations for which absorption prevails over refraction. When refraction becomes significant, the flux at all wavelengths shorter than 4 μm is already absorbed in gaseous bands or by haze.

The full set of lightcurves can be represented as a 2D-image (Fig. 4). Each horizontal cut of this image represents a transmission spectrum at a given altitude. Each vertical cut is a lightcurve at a given wavelength. Note the conspicuous molecular bands at specific wavelengths, superimposed on a general continuous absorption by hazes. As expected, aerosols have larger extinction at shorter wavelengths, so that the light decreases at higher altitudes near 1 μm than near 5 μm.

3.3. Spectra retrieval

Each spectrum must be divided by the solar spectrum observed free of atmospheric absorption to yield a normalized transmission spectrum. In this manner, only absorptions by atmospheric components appear in the transmission spectra.

The most accurate reference solar spectrum is the one acquired just after egress, when the Sun was observed through the same optical system as during the occultation. As this method deals with relative measurements, data does not need to be calibrated before the division. Thus we eliminate uncertainties on instrumental calibration. The solar reference spectra is computed as the mean of the 49 spectra between 1000 and 2000 km, that is in the same altitude range used for the slope correction.

Each spectrum is divided by this solar reference spectrum to obtain the transmission spectra. 63 spectra (cubes V1516019443_1.QUB to V1516019894_1.QUB) are kept and are analyzed here. Representative spectra are presented in Fig. 5.

The 49 spectra used to calculate the solar reference spectrum are also used to estimate the noise of the data. This estimation is done in each of the four order-sorting filters of the VIMS-IR instrument. However, two noise levels were defined in the fourth filter because we note that the last 39 channels ([4.80–5.12] μm) are noisier than the other channels of this filter. The standard deviation of each spectrum is calculated and the mean over the 49 values is kept. The rms-noise level in each interval is 6.2×10^{-3} in [0.88–1.60] μm, 3.6×10^{-3} in [1.67–2.95] μm, 7.5×10^{-3} in [3.03–3.83] μm, 27.1×10^{-3} in [3.90–4.79] μm, 81.1×10^{-3} in [4.80–5.12] μm. These values are used in all the χ^2 tests for the least square fits presented later.

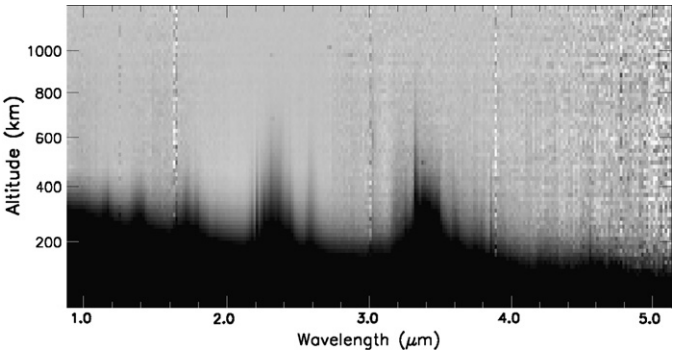

Fig. 4. 2-D plot of the full set of egress data. Each horizontal cut is a spectrum at a given altitude. Each vertical cut is a lightcurve at a given wavelength. The molecular absorption bands are visible as vertical dark patterns. The slope of the limit between dark areas and bright areas indicates that haze absorption begins at higher altitudes at the shortest wavelengths.

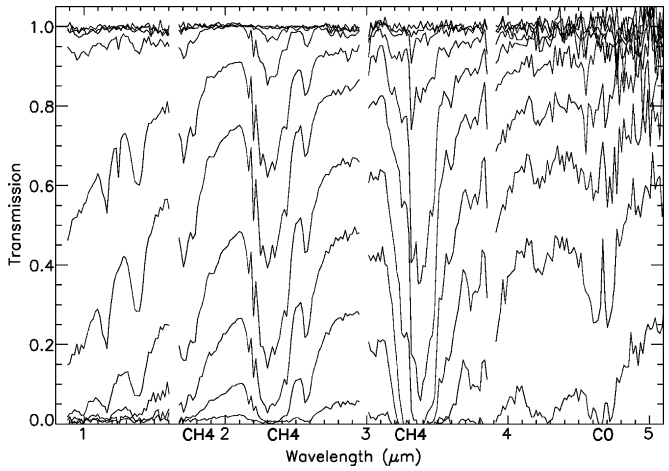

Fig. 5. 10 transmission spectrum observed at 987, 762, 586, 422, 286, 217, 164, 127, 92, 59 km. Note the decrease of the continuum level as altitude decreases. The gaps in the spectra correspond to the 3 filter gaps of the instrument.

4. Modeling of molecular absorption bands

Various molecular absorption bands can be seen in the spectra displayed in Figs. 4 and 5. Methane bands clearly appear under 800 km altitude, while CO shows up under 180 km, besides other features discussed below.

Gas absorption has been modeled by radiative transfer methods, using a line-by-line method in spherical geometry (see details below). Line-by-line model is preferred to band models because of a higher accuracy in the well-studied 2.3 and 3.3 μm domain. Only absorption is taken into account, i.e. no refraction or scattering is included. The abundance of the studied component is the only free parameter. Theoretical transmission spectra were calculated for a large range of abundances in order to find the one that best fits the data.

4.1. The model

In situ measurements by the *Huygens*/HASI instrument are used to model the atmosphere below 1000 km (Fulchignoni et al., 2005). Temperature, altitude and pressure profiles were retrieved from the Planetary Data System. The HASI temperature profile measured at 10° S is slightly different from the temperature profile at 71° S. However, comparison to results obtained with CIRS measured temperature profiles has shown that no significant differences appear. The density of gas particles is derived from the ideal gas law. The atmosphere is divided in layers of decreasing thickness with altitude. This thickness is calculated so that the horizontal path in each layer is a constant number, dS. To model the absorption along the line of sight reaching z_0 at the limb of Titan, the atmosphere above z_0 is divided into L layers of thickness $dz(i) = z(i) - z(i-1)$, $i = 1, L-1$, so that:

$$dS(i) = \sqrt{\big(R + z_0 + z(i)\big)^2 - (R + z_0)^2} - \sqrt{\big(R + z_0 + z(i-1)\big)^2 - (R + z_0)^2},$$

where R is Titan's radius.

Using vertical temperature profile $T(z_0)$, the gravitational factor $g(z_0)$ varying with altitude, the Boltzmann constant k_b, and the mean molecular weight M of the atmosphere, the scale height, $H(z_0) = k_b \times T(z_0)/M \times g(z_0)$, is calculated at each altitude. $H(z)$ is averaged above z_0 to give H, an intermediate parameter used to define the size of the layer. The horizontal paths $dS(i)$ are then fixed to a constant fraction of H, $dS = H/\alpha$, where α is a prescribed parameter. The absorptions we want to calculate depend on the column density integrated over the line of sight which is a quantity that must not depend on the number or the size of the layers. The integrated column density is calculated for different values of α. It appears not to vary significantly for α equal or greater than 7. Thus dS is fixed to the value $dS = H/7$, which is the largest size of the layers that ensures a correct calculation (that is a result that does not depend on the layering of the atmosphere) without spending too much computing time. One can note that the altitudes $z(i)$ are changing with the value z_0 of the minimum altitude, but that does not affect the results.

With this layering of the atmosphere, the number of layers is $N = 389$ for a light ray passing at $z_0 = 49$ km above the surface, $N = 218$ for $z_0 = 421$ km, $N = 25$ for $z_0 = 987$ km.

4.2. Molecular data base

The composition of the atmosphere in our model is 98% N_2 (volume mixing ratio), a fixed value of 4.35×10^{-5} of Ar (Niemann et al., 2005) and a varying value for CH_4. When modeling the 4.7 μm CO band, a value of 1.6% of CH_4 (CIRS value) is used in the computation of the mean molecular mass of the atmosphere. However these particular values have little effect on the final result, since the mean molecular mass of the atmosphere is only used in the computation of the scale height, which is used in turn in the definition of the atmospheric layering.

Three band systems of CH_4 are modeled: the $\nu 3$ system at 3.3 μm, the $\nu 3 + \nu 4$ system at 2.3 μm and the $2\nu 3$ system at 1.7 μm. The lines lists we used are issued from the work done in Dijon University (Boudon et al., 2004). They include $^{12}CH_4$ for these three bands and $^{13}CH_4$ for the 3.3 μm band (with an isotopic ratio $^{12}C/^{13}C = 82.3 \pm 1$; Niemann et al., 2005). A Voigt profile was adopted for each line. The Lorentz broadening coefficients due to CH_4–N_2 collisions in the three methane bands are respectively 5.3×10^{-2} cm^{-1} (1.7 μm), 5.7×10^{-2} cm^{-1} (2.3 μm) and 6.0×10^{-2} cm^{-1} (3.3 μm). A Lorentz halfwidth of 4.8×10^{-2} cm^{-1} was used for CH_4–Ar collisions broadening for the three methane bands (Jacquinet-Husson et al., 2005). Finally, the exponent for the T dependences are 0.6 for N_2 and 0.05 for Ar, respectively.

To model the CO absorption band at 4.7 μm, we used the line list from GEISA database (Jacquinet-Husson et al., 2008) that includes all the isotopes of CO. We include CH_3D as this molecules has absorption lines in the wings of CO. Their absorptions are computed simultaneously. A 6.5×10^{-2} cm^{-1} Lorentz halfwidth was used for CO–CH_4 collision broadening with a $T^{-0.75}$ dependence.

The high-resolution spectra resulting from line-by-line calculations are then convolved with a set of Gaussian functions, where the FWHM equal those of the 256 individual spectral channels of the VIMS instrument.

4.3. Results on CH_4

Since the Voyager 1 encounter, N_2 is known to be the major constituent of Titan's atmosphere, followed by methane, which amounts to a few percent of the composition. However, the CH_4 abundance was not precisely determined before the *Cassini* and *Huygens* measurements. The Gas Chromatograph Mass Spectrometer (GCMS) on board the *Huygens* probe made *in situ* measurements of the atmospheric composition (Niemann et al., 2005), yielding a CH_4 mole fraction of $(1.41 \pm 0.07) \times 10^{-2}$ in the stratosphere, at an altitude range of 60 to 140 km. A rapid increase of the mole fraction is observed below 32 km, where it reaches 4.92×10^{-2} at about 8 km, and then stays constant below that level. Stratospheric measurements by the CIRS instrument indicates a CH_4 mole fraction of $(1.6 \pm 0.5) \times 10^{-2}$ (Flasar et al., 2005). A consensus on the CH_4 stratospheric abundance has been established around 1.4–1.6%. We cannot re-improve this mixing ratio here. Instead, we validate our method on the methane abundance and then apply it to the CO molecule for which the abundance is much less constrained.

As the VIMS-IR spectrometer covers a wavelength range from 0.8 to 5.1 μm, we can observe several CH_4 bands, at 1.15, 1.4, 1.7, 2.3 and 3.3 μm. The central features of the 3.3 μm band appears just below 800 km. The 2.3 μm band appears at about 700 km and the 1.7 μm band at about 500 km.

Our radiative transfer code was used to model these 3 bands with an abundance of CH_4 varying from 1 to 2.5%. Although other bands are identified, they are not modeled as precise line lists for 1.15 and 1.4 μm CH_4 bands are not yet available for line-by-line calculations. A selection of transmission spectra with models of these three bands (1.7, 2.3 and 3.3 μm) with 1.6% of CH_4 is presented in Fig. 6.

There is a general agreement between our model and the VIMS spectra, especially for the 2.3 μm CH_4 band. Below 480 km, there is a large discrepancy between the model and the observations for the 3.3 μm band because of an additional absorption (see below). The agreement between the model and the observations of the 1.7 μm band is not as good as for the 2.3 μm. But this discrepancy might be due to the lack of accurate laboratory data for this band. We will therefore concentrate on the model of the 2.3 μm CH_4 band. An enlargement on this band at several altitudes with the models at 1.4, 1.6 and 2.0% is presented in Fig. 7. The differences between these predicted spectra are small compared to the uncertainty of the data. Although consistent with previous results, our measurement is not sensitive enough to improve the error bars for the CH_4 abundance already given by other experiments.

A least square fit is performed to determine at each altitude the mixing ratio of CH_4 that best fit our observations of the 2.3 μm band. These values are represented as a vertical profile in Fig. 8.

This figure indicates that under 200 km, a mixing ratio of more than 2% would be necessary to adjust the depth of the 2.3 μm band. This increase is unrealistic as the vertical profile of CH_4 is known to be uniform in the stratosphere, as shown by HASI and theoretical models. However, the small differences

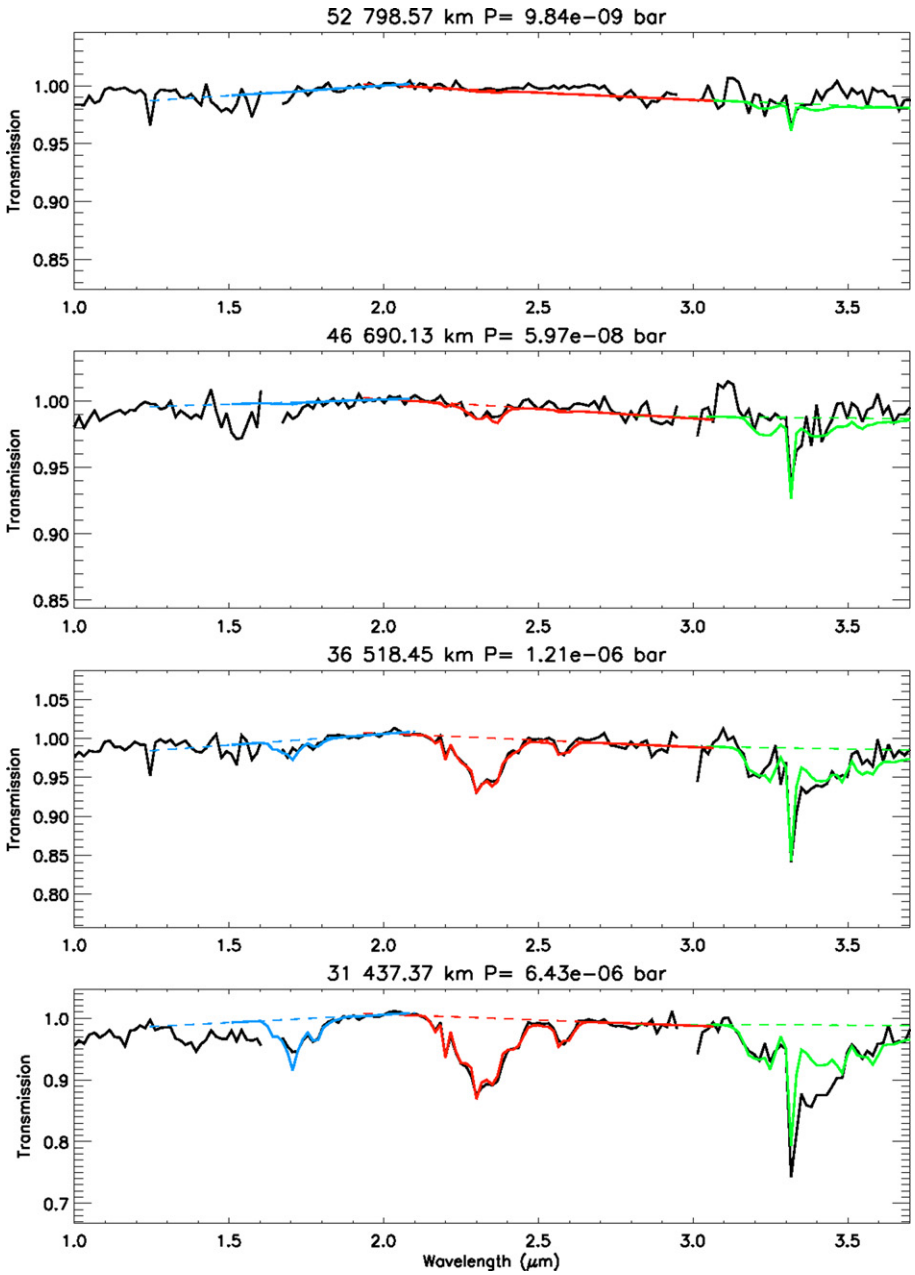

Fig. 6. (a–b) 8 transmission spectra at different altitudes (black solid lines). The color solid lines correspond to models of each bands with 1.6% of CH_4. The 1.7 μm band is in blue, the 2.3 μm band in red and the 3.3 μm band in green. The dashed lines correspond to the continuum level used for each band.

between each model, as shown in Fig. 7, reveals that our data are not very sensitive to variation of methane abundance of a few tenth of percent. This increase of the CH_4 abundance below 200 km is a systematic effect that we also observed in other occultation data sets. Our model has been carefully tested and compared to other existing models. So we do not think this increase is due to a modeling or instrumental effect. However, it could be due to a haze effect, especially because the haze density is important at these altitudes. It could be an optical effect of the haze, such as diffraction, that makes the path in the atmosphere longer than what we considered. It could be an absorption band of the haze mixed with CH_4 so that the observed band is deeper that a methane only band. It could also be due to a refractive effect. The refractivity of a gas changes in the absorption bands of this gas but this variation has not been taken into account in our calculation of the refraction. This effect might be negligible but it is difficult to quantify it. However, above 200 km, our observations are well fit with mixing ratios between 1.4 and 1.7%. These values are in good agreement with previous measurements by *Huygens* and CIRS (e.g. Niemann et al., 2005; Flasar et al., 2005).

4.4. Unknown absorption mixed with CH_4

The CH_4 3.3 μm band cannot be modeled, since an additional absorption is superimposed on the methane absorption. This feature is centered at 3.4 μm and appears under 480 km and the observed absorption is deeper than the CH_4 absorption itself. From the actual knowledge of Titan's atmosphere composition, no reasonable gaseous candidate can be found to explain this deep absorption at this wavelength. Instead, we attribute that feature to the signature of solid particles present in the atmosphere.

Observations by VIMS of a Procyon occultation through Saturn's atmosphere show a similar feature (Nicholson et al., 2006). Be-

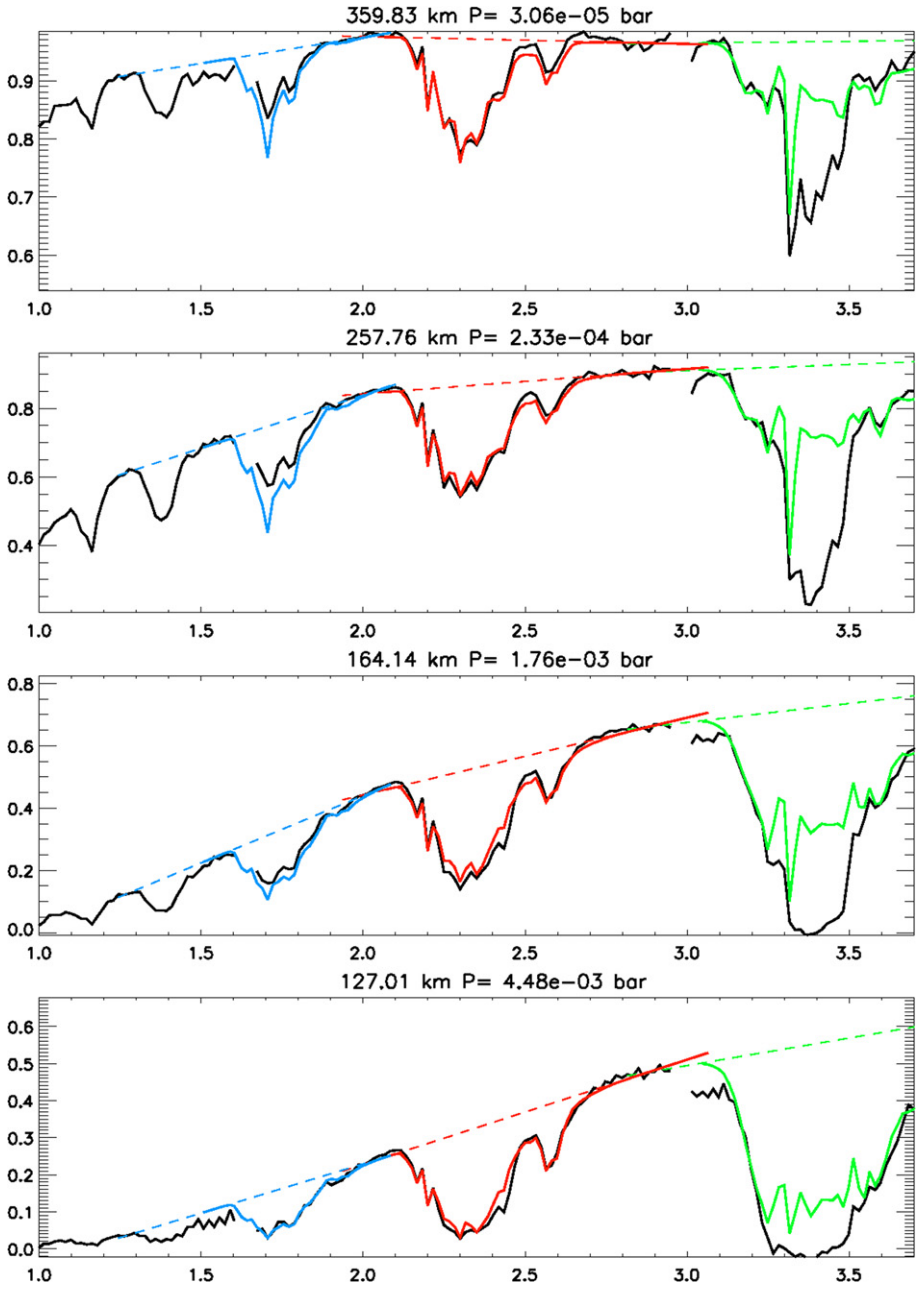

Fig. 6. (*continued*)

cause of the low abundance of nitrogen in Saturn's stratosphere, this observation suggests that the observed component might not be a nitrogenous compound. The Titan and Saturn features are over-plotted in Fig. 9. It can be seen that there are very similar, although the fine structure at the bottom of the band is slightly different.

The strongest absorption of the Titan feature is found in the 16.5 nm wide channel centered at 3.3656 μm (2971 cm^{-1}). For the Saturn feature, the strongest absorption is found in the same spectral channel at high altitude ($P < 10^{-2}$ mbar) but for the spectra at the deepest altitudes ($P > 10^{-2}$ mbar), the peak is found in the 16.5 nm wide channel centered at 3.4155 μm (2928 cm^{-1}). A shoulder spread on the two spectral channels centered at 3.4487 and 3.4648 μm is seen in both data sets, but is more evident in the Titan data.

A similar absorption is observed since more than 20 years in the Interstellar Medium (ISM) (Sandford et al., 1991; Pendleton, 1999; Pendleton and Allamandola, 2002). This feature is considered as a tracer of the solid state organic component of the diffuse interstellar medium (DISM). This 3.4 μm band probes the C–H stretching mode of aliphatic hydrocarbons. However, this band does not provide much information about what these aliphatic chains may be attached to. In the ISM, these chains are supposed to be attached to large organic molecules. The different stretching modes (asymmetric or symmetric) of $-CH_2$ and $-CH_3$ groups determines the position and shape of this absorption. The asymmetric C–H stretching of $-CH_3$ and $-CH_2$ groups are characterized by subpeaks at 3.385 μm and 3.42 μm respectively (Sandford et al., 1991; D'Hendecourt and Allamandola, 1986). With a mean resolution per spectral channel of 16.6 nm for VIMS instruments, there is a good agreement between the observed position of the observed subpeak and the laboratory values. Laboratory values are measured for saturated unbranched hydrocarbons of general formula $CH_3-(CH_2)_n-CH_3$. On Titan, such molecules are gases or liquid for n

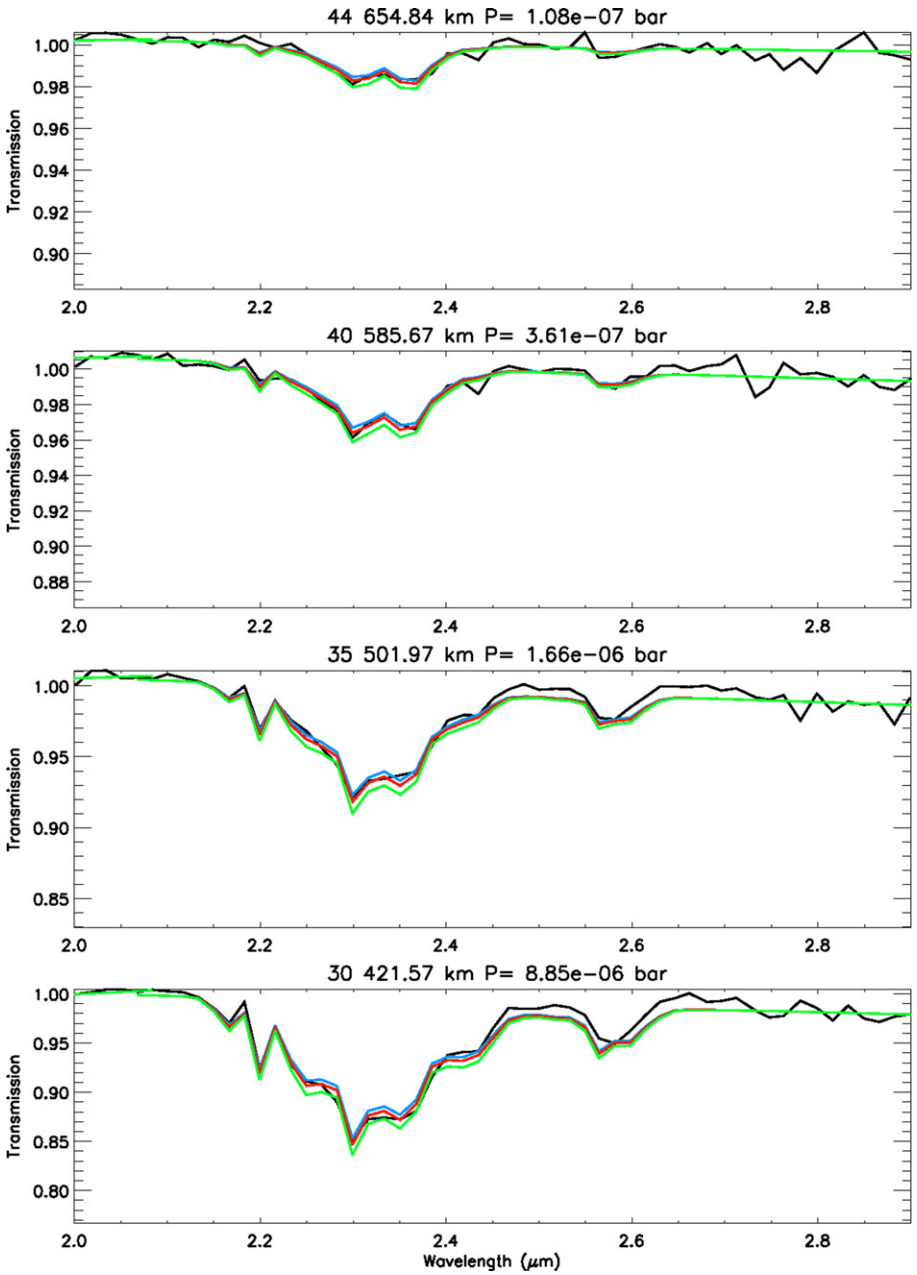

Fig. 7. (a-b) Enlargement of the 2.3 μm band at the same altitudes as in Fig. 8. Observations are in black. Solid color lines represent models with 1.4% (blue), 1.6% (red) and 2% (green) of CH_4.

up to 10. But we suppose that the observed feature comes from aliphatic chains attached to larger molecules. If electronegative groups (OH, NH) were associated close to the $-CH_3$ and $-CH_2$ groups, the observed peaks would be shifted to shorter wavelengths from their nominal positions. So that OH or NH groups might not be chemically bond adjacent to the C–H bond responsible for the observed feature. We may also note in passing that the signature for symmetric C–H stretching is at 3.48 μm which is slightly beyond the position of the observed shoulder.

As the $-CH_3$ stretch feature is more visible than the $-CH_2$ one in Titan data, that might suggest quite short aliphatic chains. In Saturn's atmosphere, the main peak is at the position of the $-CH_3$ stretch at high altitudes and at the $-CH_2$ stretch position at the lowest altitude. This might suggest the aliphatic chains are longer at deeper altitudes.

However, this analysis is preliminary. The VIMS spectral resolution is not high enough to draw assertive conclusions. The observation of this absorption with higher spectral resolution is necessary to study the structure of this feature, enable the measurement of the CH_2/CH_3 ratio and thus give indications on the length of the observed aliphatic chains.

Many lab experiments have been performed to identify the observed feature in the DISM (Pendleton and Allamandola, 2002). It should be useful to compare precisely these data to our own observation. The visual comparison indicates that some of these laboratory-produced materials could match our feature. The needed precise comparison of our data with laboratory spectrum is left for future work.

Finally, it might be possible that the material producing this 3.4 μm feature has weaker overtones in the 2.3 μm band. We have considered so far that this band is only due to methane. But such an overtone would explain the apparent rise of the methane mixing ratio. In Figs. 6a and 6b, we can see that at the altitudes where our model underpredicts the depth of the 2.3 μm band, our model

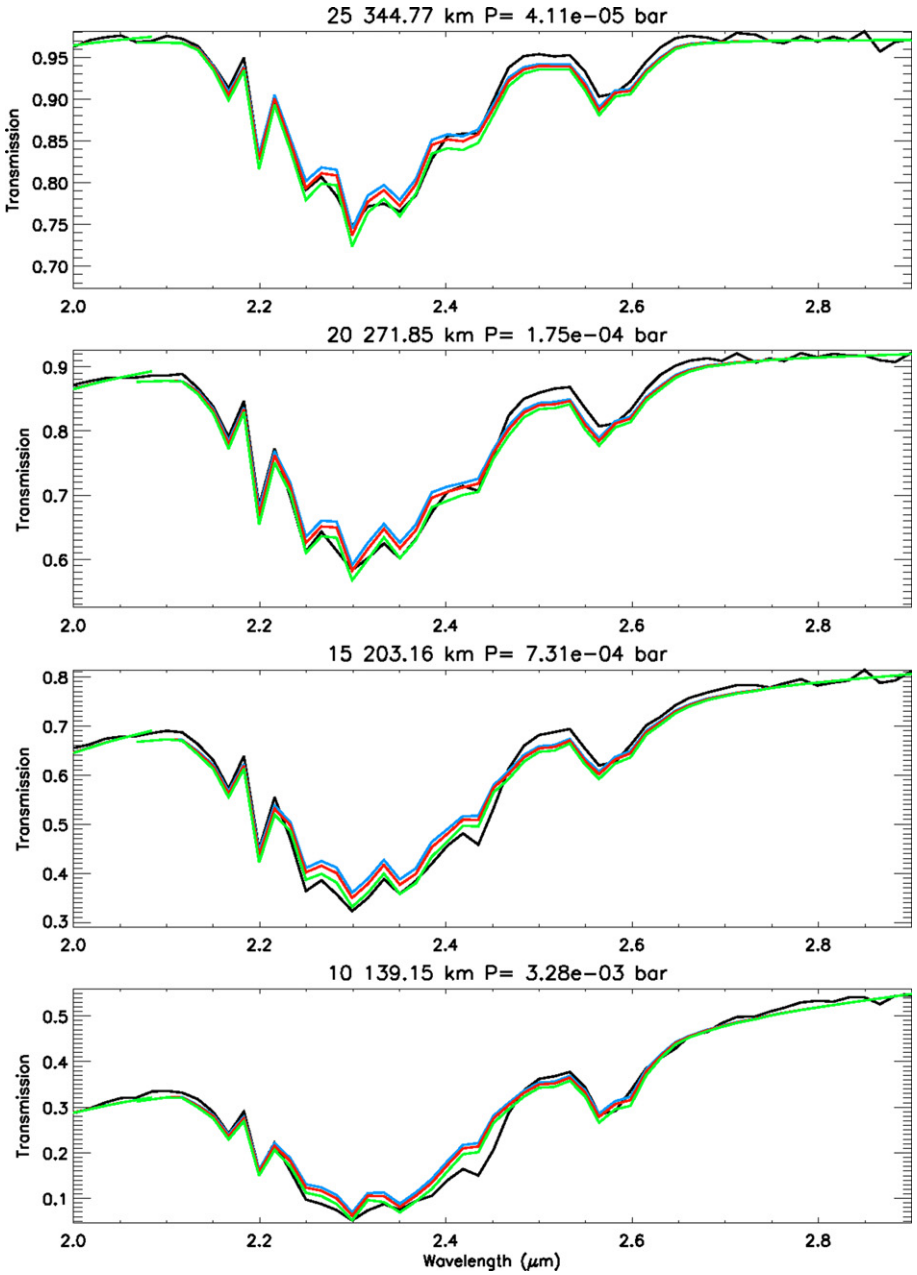

Fig. 7. (*continued*)

overpredicts the depth of the 1.7 μm band. An additional absorption in the 2.3 μm band under 300 km would thus decrease the CH_4 ratio needed to fit the data in this altitude range.

4.5. Results on CO

Carbon monoxide was first detected in Titan's atmosphere by Lutz et al. (1983), with a mixing ratio of 60 ppm. The CO photochemical lifetime in Titan's atmosphere is about 500 Myrs to 1 Gyrs (Lellouch et al., 2003; Wong et al., 2002), much longer than the typical transport timescale (160 yrs for a typical eddy diffusion coefficient of 1000 $cm^2\,s^{-1}$). Note that CO has the same molecular weight as N_2, the most abundant gas, and that the temperature is never low enough for CO to condense. Thus CO should be uniformly mixed throughout Titan's atmosphere. The CO vertical profile is important because it addresses the question of an internal or an external origin for CO. Actually, if CO were only formed by oxygen photochemistry, its abundance would be much lower than data currently published. The steady state was found to occur at CO = 10 ppm in Lara et al. (1996), and at only 1.8 ppm in Wong et al. (2002).

Many observations with different techniques have been made to determine the CO abundance. A tropospheric measurement comes from VLT observation by Lellouch et al. (2003) in the 5 μm window and indicates a 32 ± 10 ppm for CO/N_2 mixing ratio. Observations by Hidayat et al. (1998) indicates a CO mixing ratio decreasing with altitude: 29^{+9}_{-5} ppm at 60 km, 24 ± 5 ppm at 175 km and $4.8^{+3.8}_{-1.5}$ ppm at 350 km. Observations of the CO fluorescence by López-Valverde et al. (2005) support the tropospheric value of 32 ppm and indicates an increase to 60 ppm in the stratosphere. This latter value is consistent with successive values published by Gurwell and Muhleman (1995, 2000), and by Gurwell (2004). Their observations are presented as evidence of a well mixed vertical profile with a mixing ratio of 50 ± 10 ppm (Gurwell and Muhleman, 1995), 52 ± 6 ppm (Gurwell and Muhleman, 2000), and

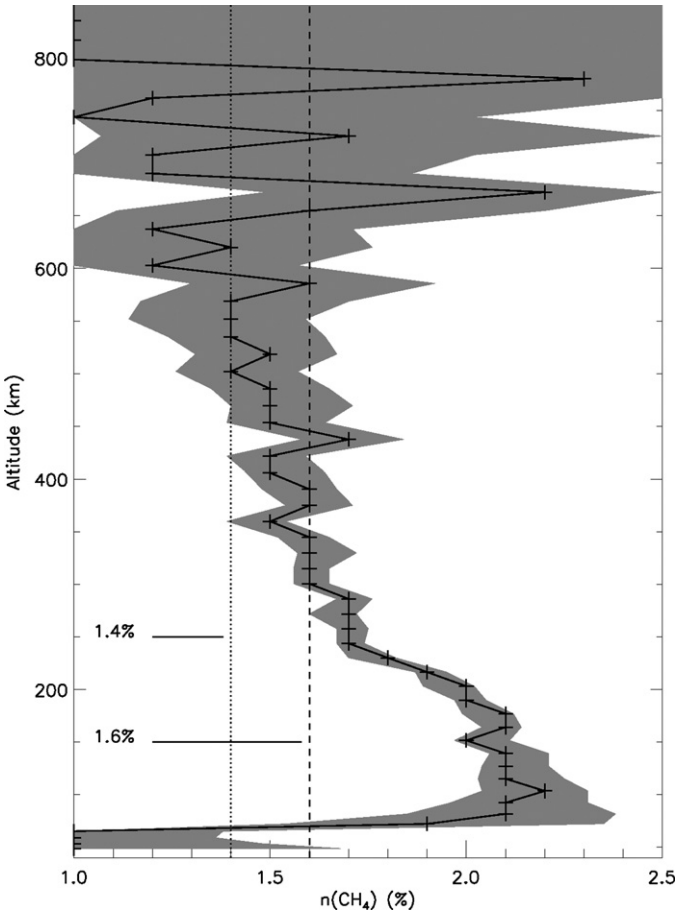

Fig. 8. At each altitude, abundance of CH_4 that best fits the observed 2.3 μm band in a least square sense (solid black line). The gray area represents the 3-σ error bars. Vertical lines corresponding to 1.4 and 1.6% abundances of CH_4 are represented for comparison with our fit.

Table 1

Altitude	Nominal value ±3-σ error
127 km	28^{+12}_{-8} ppm
115 km	$22^{+8.5}_{-2}$ ppm
103 km	$30^{+7.5}_{-6.5}$ ppm
92 km	$32^{+6.5}_{-6}$ ppm
82 km	$52^{+11.5}_{10}$ ppm
72 km	$38^{+11.5}_{-9.5}$ ppm

51 ± 4 ppm (Gurwell, 2004). Space observations by the CIRS instrument on *Cassini* indicate a mole fraction of 45 ± 15 ppm (Flasar et al., 2005) and 47 ± 8 ppm (de Kok et al., 2007). Nighttime emissions of CO were discovered by the VIMS instrument and indicate an abundance of 32 ± 15 ppm (Baines et al., 2005, 2006).

In our occultation data, the 4.7 μm absorption band of CO is seen at altitudes below 180 km (it is not detectable above that altitude due to noise). Our model assumes a uniform mixing ratio with values between 10 and 80 ppm with steps of 2 ppm. Because CH_3D has absorption lines in the shorter wavelength wing of the CO band, it was included in the calculation with an abundance of 7.5×10^{-6} as published in Coustenis et al. (2007).

The continuum level was estimated using data points in the intervals 4.132–4.166 μm (3 points), 4.448–4.466 μm (2 points), and 5.006–5.123 μm (8 points). Values in the second interval were corrected for CH_3D absorption. A linear fit to these 13 points was made and the results taken as the continuum level. A second order polynomial fit was also used to evaluate the impact of the continuum level on the determination of the CO abundance. Observations and models are presented in Fig. 10.

The mixing ratio of CO was evaluated on 6 spectra between 127 and 72 km using a least square method. The χ^2 tests were performed on the 24 points spanning the CO band. The noise of the data in this wavelength range was estimated using spectra at higher altitudes as described above. The rms deviation is $\sigma = 27.1 \times 10^{-3}$ in [3.90–4.78] μm and $\sigma = 81.1 \times 10^{-3}$ in [4.80–5.12] μm intervals. Individual measurements are presented in Table 1 with their 3-σ error bars. The measured value in the spectrum at 82 km altitude is quite far from the other ones because of noisier data points. Using those six values, the mean value for CO mixing ratio is 33.6 ppm with a formal error bar of ±3.6 ppm. However, one can note that individual measurements are more scattered that this theoretical error. Furthermore, when using a second order polynomial fit to estimate the continuum, the mean value of CO mixing ratio is 29.7 ppm with individual error bars between 6 and 12 ppm. A reasonable estimate of the CO mixing ratio from this data set is thus 33 ± 10 ppm. Our measurement represents the abundance of CO in the lower cold stratosphere, in the altitude range 70 to 130 km. The absorption band is seen in our data above 130 to 180 km, but they are too noisy to be included in the fit. So that no conclusion on the abundance can be drawn from the detection of CO at these altitudes. Our model with uniform mixing ratio predicts that absorption by CO should be visible up to 300 km, but this faint absorption is then dominated by noise. In other words, if a CO absorption is present between 180 an 300 km, we cannot detect it with the signal-to-noise ratio of our data.

In this work, the observation of the CO absorption in the lower cold stratosphere yields a CO mixing ratio in good agreement with the value measured with the observation of CO nighttime emission in the upper warm stratosphere (200–300 km; Baines et al., 2006). The CO abundance presented here is also in very good agreement with CIRS measurements in the same altitude range (Flasar et al., 2005; de Kok et al., 2007). Tropospheric measurements from Earth based observations are also in the same range of value (Lellouch et al., 2003; López-Valverde et al., 2005). These different observations, probing different altitude ranges, all yield similar values of the CO mixing ratio, so that CO appears to be relatively constant with altitude.

4.6. Another absorption

In Figs. 10a and 10b, an absorption feature is visible between 4.2 and 4.3 μm. It was first attributed as a CO_2 signature. However our radiative transfer model, using a mixing ratio of 1.5×10^{-8} according to CIRS measurements (Coustenis et al., 2007), clearly dismisses this possibility. The observed depth of this feature is about 5 times deeper than the predicted CO_2 band in Titan's atmosphere. Furthermore, this feature is located at wavelengths slightly shorter than the actual position of the CO_2 band. Therefore, the identification of this feature remains to be done.

5. Haze absorption

We now turn to the study of haze properties. We recall that egress observations are made at about 70° S in the summer southern hemisphere, i.e. far away from the winter polar hood, confined at high northern latitudes.

Comparison of the different transmission spectra taken at different altitudes shows that the continuum level of those spectra decreases with decreasing altitude. This general drop is due to the absorption by haze particles present in Titan's atmosphere, and responsible for its orange color. The "2-D" image of the occultation

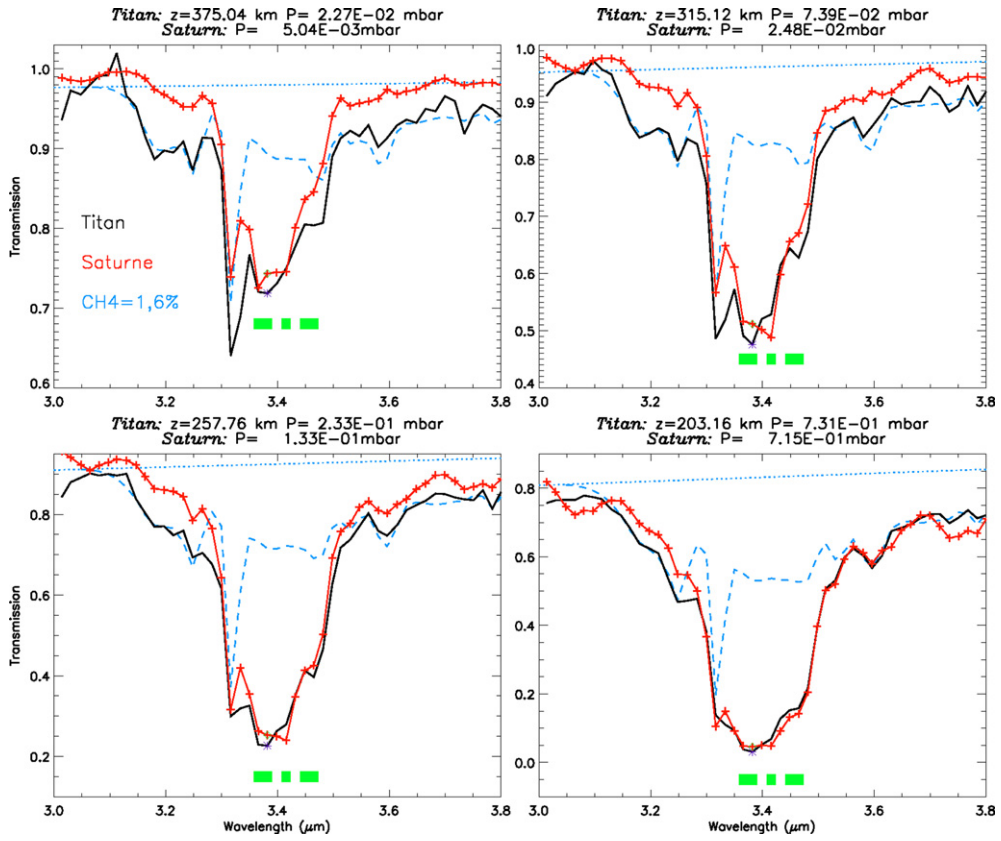

Fig. 9. Comparison between observations in Titan's atmosphere (black) and Saturn atmosphere (red) of the 3.4 μm feature. For each Titan spectrum, we overplot the Saturn spectrum the most similar in depth. Altitudes and pressures levels are indicated in the title of each figure. The blue dashed line represents the 1.6% CH_4 model of the 3.3 μm. The green squares represent the spectral channels, from left to right, channels 150–151 (3.3656–3.3818 μm), channel 153 (3.4155 μm) and channels 155–156 (3.4487–3.4648 μm).

(Fig. 4) also indicates that this absorption is more important at shorter wavelengths. That is the expected behavior for light absorption by haze particles.

Thus, in this part, we present a model of haze absorption. First, we derive a vertical profile of the extinction coefficient in continuum wavelengths. Assuming fractal aggregates for the structure of haze particles, density profiles are retrieved for different size of aggregate. Then the corresponding transmission spectra are computed and compared to observation to constrain haze structure and optical constants. In a last part, we also look at the spectral behavior of the haze and compare it to previous results.

5.1. Profile of the extinction coefficient

Along its path through the atmosphere, sunlight is attenuated by aerosol scattering by a factor $\exp(-\tau_\lambda)$, where the optical depth τ_λ is given by

$$\tau_\lambda(z_0) = \sum_{\text{all levels}} k_\lambda(i) \times ds(i) = \sum_{\text{all levels}} n(i) \times \sigma_N(\lambda) \times ds(i),$$

where $k_\lambda(i)$ is the extinction of the ith layer, $n(i)$ is the number density of haze particles in layer i, $ds(i)$ the elementary path of the light in that layer along the sunlight's path, and $\sigma_N(\lambda)$ the scattering cross-section of the aggregate. The optical depth is derived from the observed spectra; thus, the extinction is the only unknown in this set of $N_s = 63$ equations (corresponding to the 63 spectra), one for each data cube/altitude.

The atmosphere is divided in 63 layers corresponding to the 63 altitudes probed, with altitudes increasing with i. Layer i is between $z_0(i)$ and $z_0(i+1)$ and the 63th layer expands up to 1000 km. The main assumption is that the extinction is constant within each layer. This is reasonable as the 63 layers are each less than 20 km thick. We note here that this vertical sampling is smaller than the resolution of each cube (50–60 km, see Section 3). The inversion begins at the altitude $z_0(i_{\text{top}} = 55) = 854$ km. We assume that above that level,

$$z_0(i \geqslant i_{\text{top}}), \quad k_\lambda(i) = k_\lambda(i_{\text{top}}) \times \exp\left(-\frac{z_0(i) - z_0(i_{\text{top}})}{H}\right),$$

where the scale height $H = \frac{RT}{mg} = 62$ km, with $T(800\text{ km}) = 160$ K, $m = m_{N_2} = 28\ \text{g mole}^{-1}$ and $g(800\text{ km}) = 0.76\ \text{m s}^{-2}$. Using the observed transmission at 854 km, $k_\lambda(i_{\text{top}})$ is calculated. The values of $k_\lambda(i)$ for $i < i_{\text{top}}$ are then determined using the transmission observed at $z_0(i)$ and the value of $k_\lambda(i')$ for i' between $i+1$ and i_{top}. This "onion-peeling" process is repeated for each observed spectrum until the $N_s = 63$ values of k_λ are computed.

This calculation is done for each VIMS spectral channel. But the relevant parts of the spectra are those in the continuum intervals, where there is no molecular absorption. We have defined 6 of those intervals, whose limits are indicated in Table 2. No data points were chosen in the continuum window around 3 μm because of the strong absorptions features in the transmission models (see Section 5.3).

The extinction profiles are presented in Fig. 11. (Note the logarithmic horizontal scale.) Some points are not defined as they correspond to negative values of the extinction. This occurs at high altitudes when the transmission can get artificially larger than unity because of noise. In Fig. 11, the extinction appears to increase exponentially below 460 km. A linear fit to $\ln(k_\lambda)$ between 77 and 461 km for continuum wavelength below 4.7 μm give values for the scale height ranging from 55 to 79 km, with a mean value of 64 km.

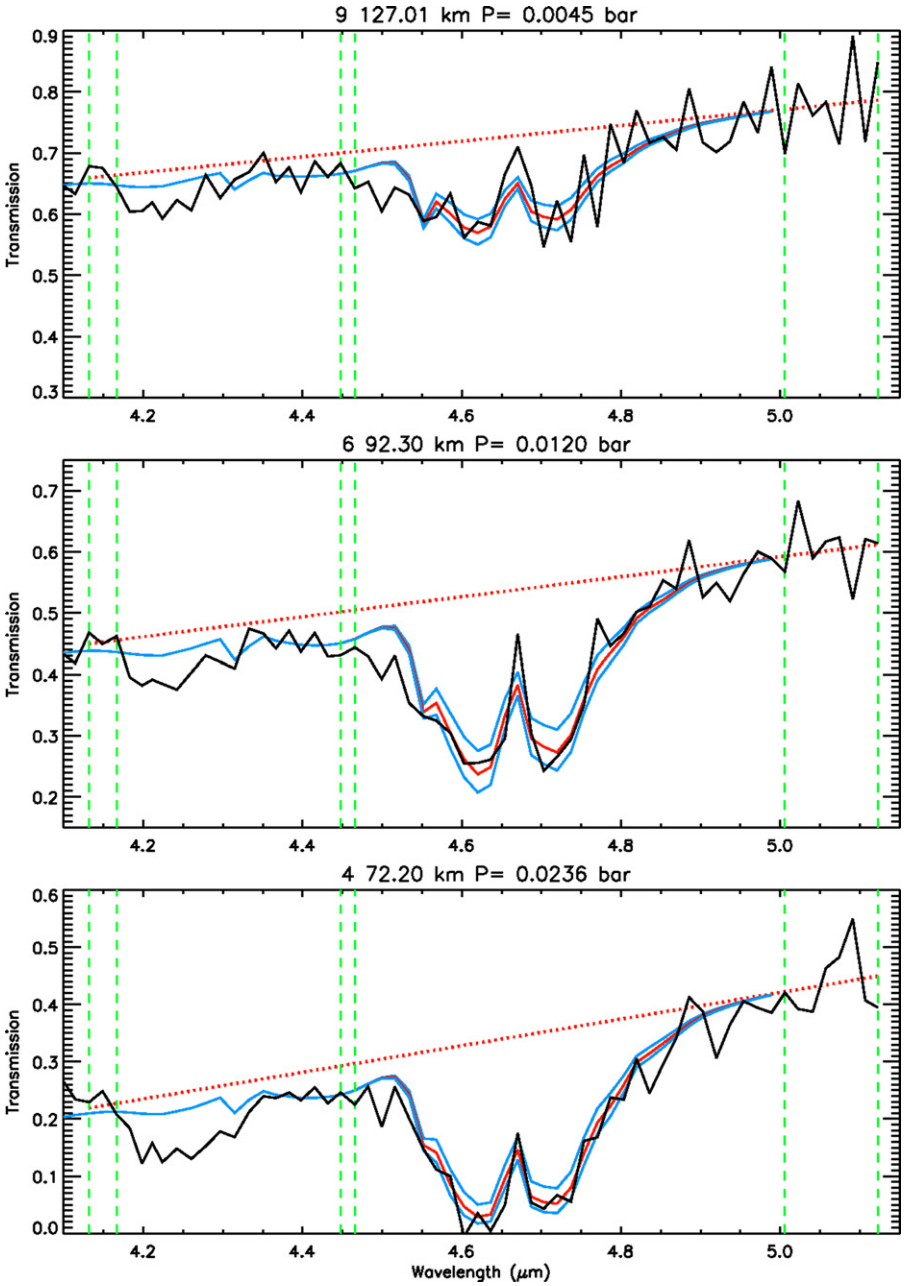

Fig. 10. Three transmission spectra of the CO 4.7 μm band at three different altitude levels (black solid line). (a) Models with a continuum (red dotted lined) estimated with a linear fit. (b) Right column presents the models with a continuum (red dotted lined) estimated with a second order polynomial fit. The model with mixing ratio of 32 ppm is represented as a red solid line. Blue solid lines represent models at 22 and 42 ppm to represent the error bar. Green dashed vertical lines represent the intervals used to estimate the continuum.

5.2. Retrieval of density profiles

Several measurements have shown that the light scattered by Titan's atmosphere is highly polarized. To explain this observation, it is supposed that aerosols are fractal aggregates of spheres. (West and Smith, 1991) The radius of these spherical monomers is constrained by DISR measurements of the phase function and degree of polarization. Tomasko et al. (2008) show that a radius of 0.05 μm or less is needed to explain DISR observations. In the same paper, the number N of particles per aggregate was found to be about 3000 above 60 km.

In our model, haze particles are aggregates of N spheres of 0.05 μm radius, with a fractal dimension $D_f = 2$ (Rannou et al., 1997). We consider ten values of the number N of spheres in each aggregate between 1 and 30,000. Each kind of aggregate is characterized by its scattering cross-section $\sigma_N(\lambda)$. They result from an optical model developed by Botet et al. (1997) and applied for Titan by Rannou et al. (1997). In 1984, Khare et al. produced laboratory analogs of Titan's aerosol that they called tholins. Real and imaginary parts of the complex refractive index of those produces were measured. These indices are the inputs of the microphysical model.

According to the previous section, the density in layer i is retrieved through $n_{N,\lambda}(i) = \frac{k_\lambda(i)}{\sigma_N(\lambda)}$. Using this equation, we have, for each spectral channel, 10 possible density profiles, corresponding to the 10 values of the number N of spheres per aggregate. As for the extinction, we only use continuum wavelengths. However, all the intervals are not relevant at all the altitudes. Only short wavelengths (<2 μm) have significant absorption at high altitudes. As the altitude decreases, longer wavelengths are also included. Then,

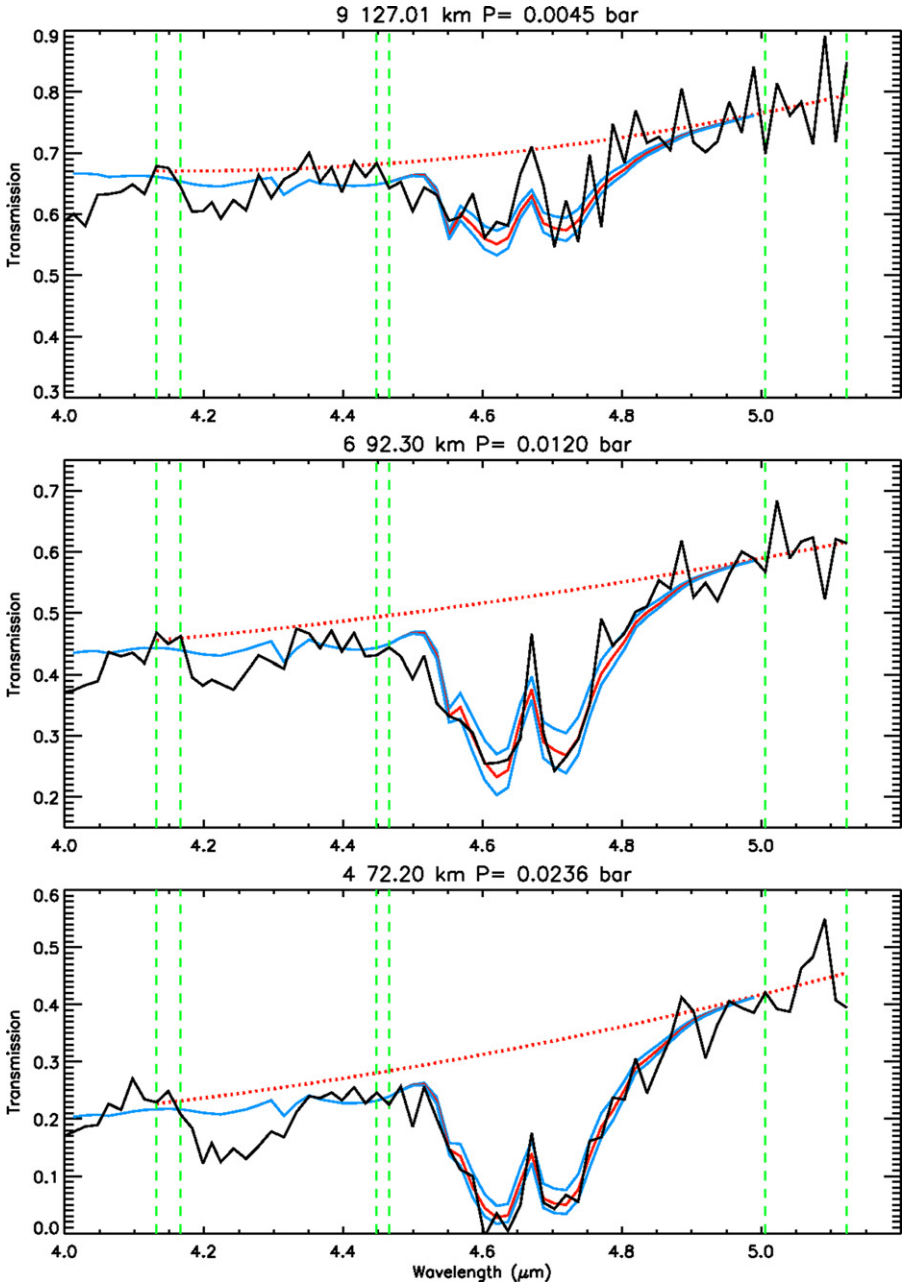

Fig. 10. (*continued*)

Table 2

Altitudes	X0 [0.88–0.9] μm (2 points)	X1 [1.08–1.11] μm (3 points)	X2 [1.24–1.29] μm (4 points)	X3 [2.00–2.10] μm (7 points)	X4 [4.13–4.17] μm (2 points)	X5 [4.45–4.47] μm (2 points)	X6 [4.97–5.12] μm (10 points)
477.5–863.5 km	×	×	×	×			
157.8–461.3 km	×	×	×	×	×	×	×
133.0–145.3 km		×	×	×	×	×	×
121.0 km			×	×	×	×	×
76.9–109.3 km				×	×	×	×

for altitudes less than 140 km, the flux at short wavelengths is completely absorbed and not taken into account. The use of each interval at each altitude is described in Table 2. In each layer, the density is the median of the values $n_{N,\lambda}(i)$ in the relevant wavelengths interval. Negative values of $n_{N,\lambda}(i)$ stemming from negative values of $k_{\lambda}(i)$ are excluded.

The 10 resulting density profiles $\tilde{n}_N(z)$, independent of the wavelength, are considered as an initial guess. At each level, we explore 371 values around this initial result, from $1 \times 10^{-4}\tilde{n}_N(z)$ to $20 \times \tilde{n}_N(z)$. The best value for the density is determined using a least square fit of the corresponding transmission models to the VIMS observations. The χ^2 test is made at each altitude and for each type of aggregate in the intervals defined above, avoiding molecular absorptions. The values of the noise used are defined in Section 4.3. We determine the density that minimizes χ^2 and the corresponding formal 3-σ error bar. The models for the trans-

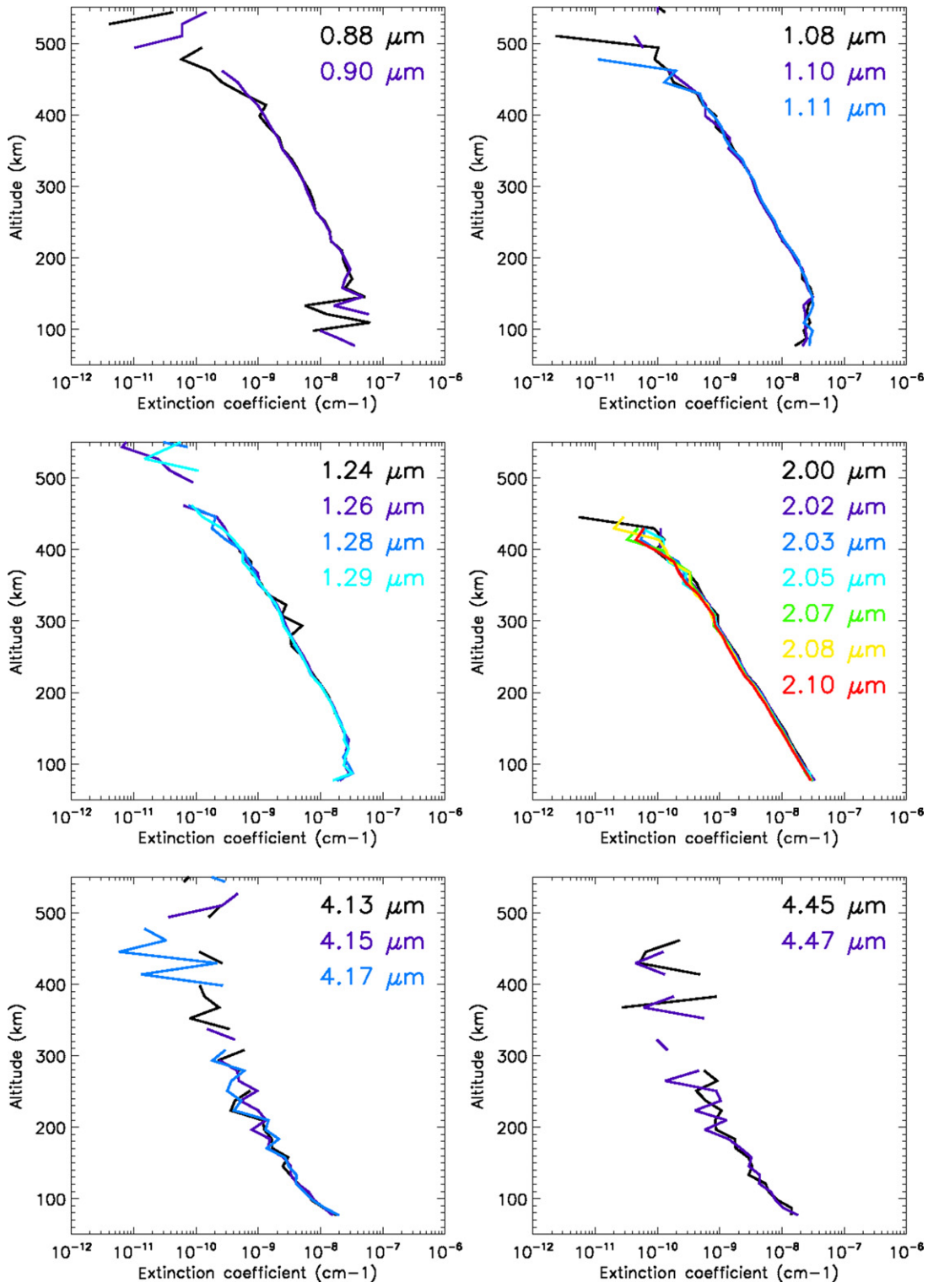

Fig. 11. Extinction profiles below 500 km in 6 wavelength intervals with no molecular absorption. The color correspondence is indicated by the legend of each plot. Note the horizontal logarithmic scale, so that the extinction appears to increase exponentially with decreasing altitude.

mission are computed iteratively, using for the altitudes above the level of interest the best densities already determined by the least square fits.

5.3. Results on transmission spectra

In Fig. 12, we overplot to the VIMS observed spectra the best fit models for several values of N. Models with less than 100 particles per aggregate are excluded right away, as it is clear that they cannot reproduce the continuum. Large numbers of particles per aggregate, typically larger than 1000, are needed to reproduce satisfactorily the observed slope of the continuum.

To improve the determination of N, we look in each layer for the value of N that leads to the smallest minimum of χ^2. Because of the uncertainty of the models above 500 km (see discussion below) we only present this result under 500 km in Fig. 13. Hor-

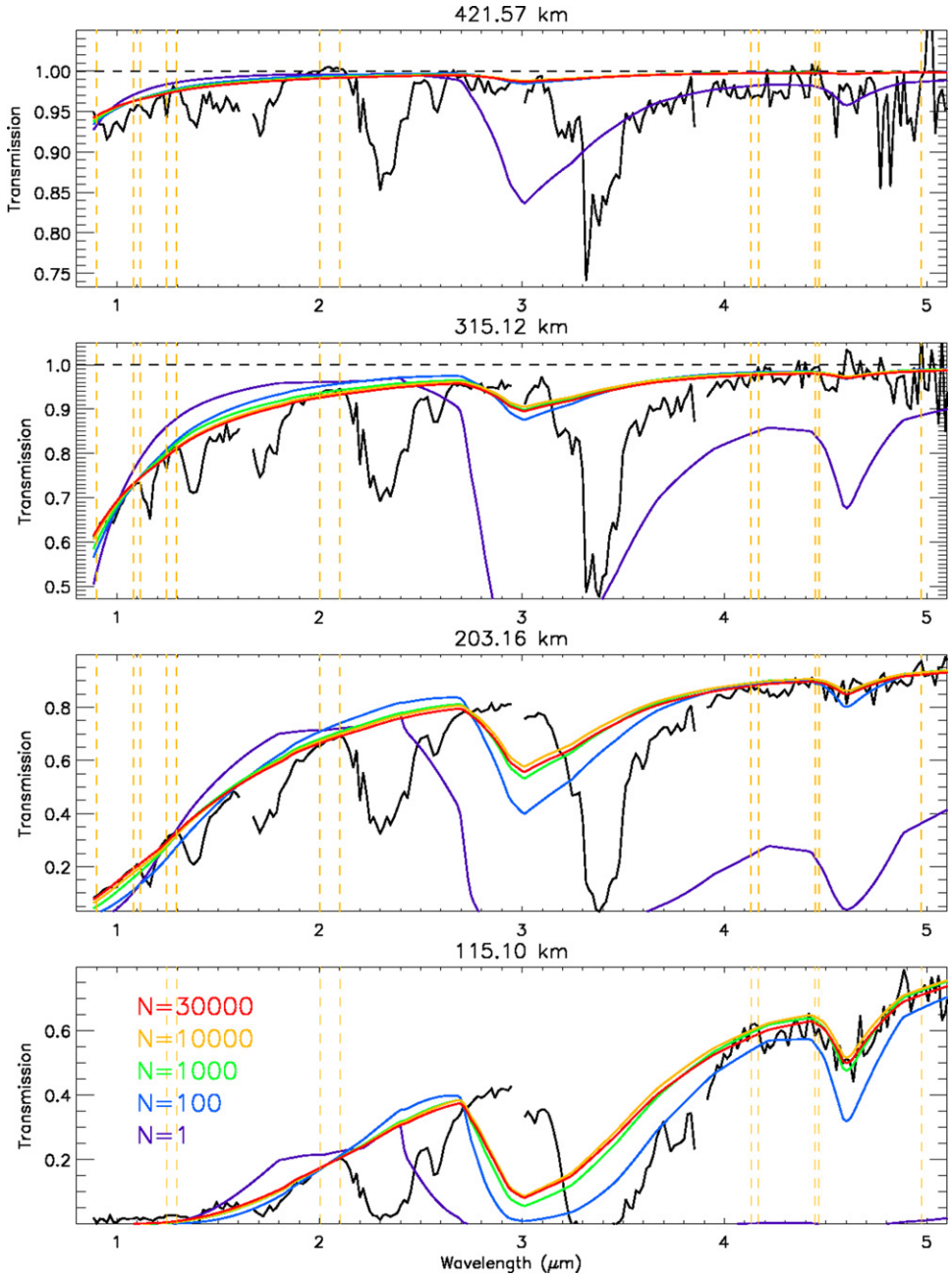

Fig. 12. VIMS transmission spectra at four different altitudes are in black. We overplot the transmission spectra of fractal aggregates with $N = 1$ (purple), $N = 100$ (blue), $N = 1000$ (green), $N = 10{,}000$ (orange), $N = 30{,}000$ (red). Each model was calculated with the density profile that best fits the data.

izontal lines represent the range of value of N with 3-σ level error-bars. This range covers all of the 10 possible values of N for altitudes above 500 km. This figure indicates once more that large values of N are more satisfactory. Our data do not allow us to determine a best number N in the interval 1000–30,000, but we can exclude values of N lower than 1000 spheres per aggregate. However, it is important to note that our near-infrared observations lead to the same conclusion as for the visual data from DISR (Tomasko et al., 2008): both data sets need large numbers of particles ($N > 1000$) per aggregates to fit the data. It must be underlined that our measurements involve higher altitudes than DISR measurements. DISR measurements are made below 150 km while our result extend up to 450 km. Finally, our results about the size of the aggregates is also in good agreement with the model developed by Bar-Nun et al. (2008) that predicted at the altitude of 100 km a number of monomer between 2400 and 2700.

Whatever the value of N, we can see in Fig. 12 that the predicted transmission spectra have two large absorption bands at 3 and 4.6 μm. They result from two peaks at those wavelengths in the refractive index of the tholins produced by Khare et al. (see Fig. 4 of Khare et al., 1984). The 4.6 μm is due to vibrational transitions of C≡N. The 3 μm is attributed to C–H bound in Khare et al. (1984) and to N–H bounds in Tran et al. (2003a) and Imanaka et al. (2004). The identification in this last paper is the most likely. Our data do not show any evidence of the 3 μm absorption. At 4.6 μm, the predicted absorption in Khare et al.'s tholins is right at the position of the CO absorption band (4.7 μm). Thus we cannot be as assertive about its absence. However, as we said before, we believe that the 3.4 μm feature observed in our data and in Saturn occultations data is a haze signature. The presence of this compound on Saturn implies that it might not contain any nitrogen. This would reinforce the non-observation of the 4.6 μm (C≡N signature) band

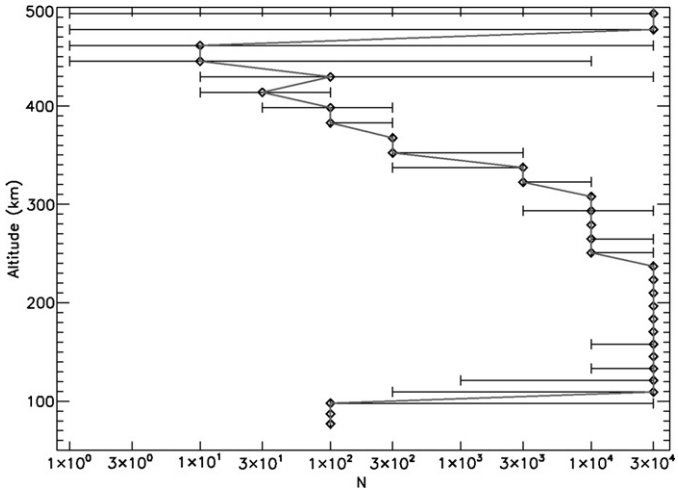

Fig. 13. At each altitude level, number N of spheres per aggregates that has the minimum χ^2. Horizontal lines represent the interval of value of N with equal probability.

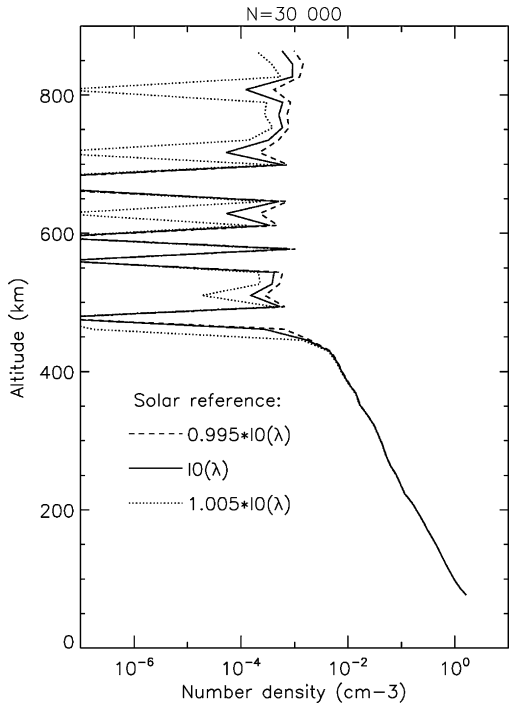

Fig. 14. Number density profile for aggregate of 30,000 spheres. The three profile were calculated using three values of the reference solar spectrum: $I_0(\lambda)$ (straight line), $0.995 \times I_0(\lambda)$ (dashed line), $1.005 \times I_0(\lambda)$ (dotted line).

of Khare et al.'s tholin in our data. These differences indicate that there are real chemical differences between the actual Titan haze and the materials called tholins produced in the lab. These differences concern the nitrogen content of the haze that must be inferior in actual haze than in Khare's tholins. This result added to the identification of aliphatic chains in the aerosols with the 3.4 μm absorption bands suggest that actual haze might have little nitrogen, such as photochemical analogs produced by Tran et al. (2003b) or Jacovi and Bar-Nun (2008).

5.4. Results on density profiles

Our inversion process begins at 854 km altitude. However, densities retrieved between 854 and 470 km are somewhat dependent on the normalization of the lightcurves. The error bars derived

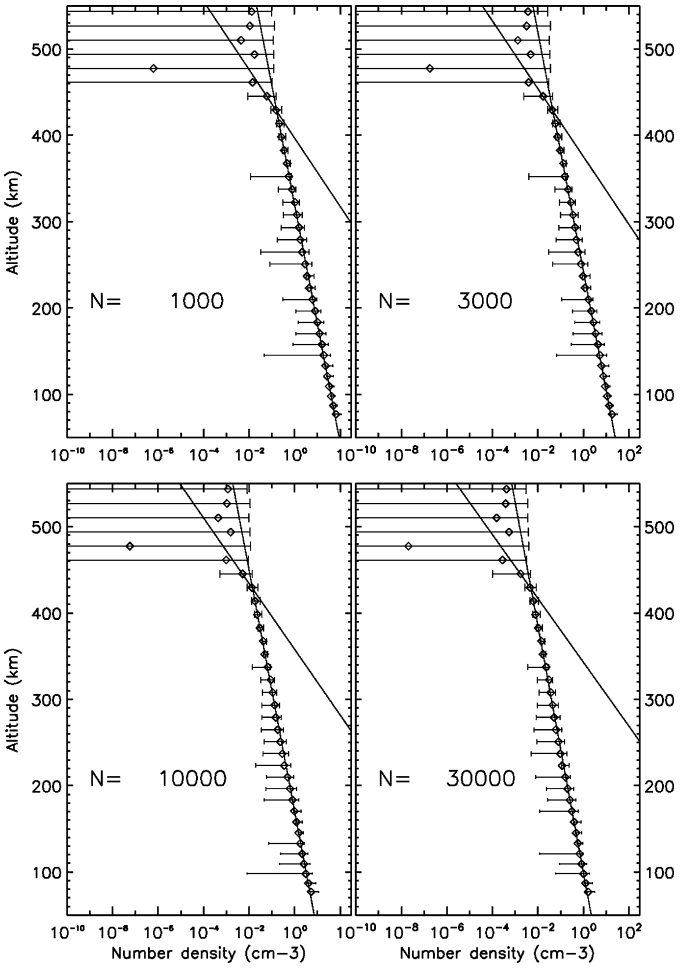

Fig. 15. Haze number density profiles fractal aggregates with four values of N. Note the horizontal logarithmic scale. The fit by $n = n_0 \times \exp(-z/H)$ for under 420 km and between 420 and 460 km are overplot (straight solid lines). The values of H are presented in Table 3.

from the least square fit of the transmission spectra are formal error bars. They underestimate the uncertainty at these altitudes. If the reference solar spectrum is modified by 0.05%, a typical value considering the quality of the data in some spectral channels, the density profile can change by more than a factor of ten above 500 km, but it is little changed under this level. This is illustrated in Fig. 14 which displays density profiles for $N = 30{,}000$ calculated with a reference solar spectrum, outside the occultation, $I_0(\lambda)$ multiplied by 1.005, 1 and 0.995, the typical error factors on $I_0(\lambda)$. This uncertainty is mainly due to the determination of $I_0(\lambda)$. The presence of some data points with transmission larger than 1, for example at about 2 μm at about 500 km, is another factor of uncertainty. That's why density profiles hereafter are only represented for altitudes lower than 500 km.

The haze density profiles with their 3-σ error bars are presented in Fig. 15. Because their transmission spectra best fit the observations, only the four profiles corresponding to values of $N = 1000$, 3000, 10,000 and 30,000 spheres per aggregate are shown. We can note on this figure that the product nN of the density and the number of spheres per aggregate is quite constant. We estimate that $nN \sim 3 \times 10^{-10}$ m^{-3} at 100 km and $nN \sim 10^{-9}$ at 300 km of altitude. This quantity is proportional to the mass density $n\rho N\frac{4}{3}\pi r^3$, with ρ is the density of the haze and r and the radius of each sphere. Assuming $\rho = 1000$ g m^{-3}, a good approximation for photochemical materials, we find values for the mass

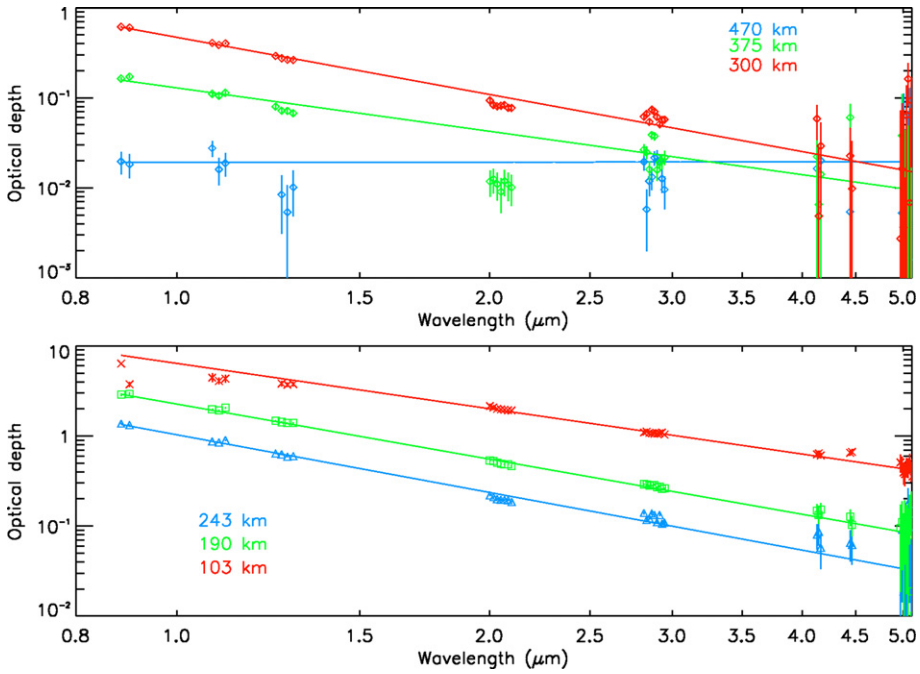

Fig. 16. Observed optical depths in continuum wavelengths for 6 altitudes levels (symbols) and fits (solid line) by an exponential law $\tau = \tau_0 \times \lambda^{-q}$. q values are plotted in Fig. 17.

Table 3

N	$H1_{\text{haze}} \pm 1\text{-}\sigma$ error 77–414 km	$H2_{\text{haze}}$ 29–461 km
1000	59.4 ± 1.5	17.2 ± 10.1
3000	59.4 ± 1.42	17.1 ± 10.1
10,000	60.1 ± 1.42	16.6 ± 10.1
30,000	61.2 ± 1.43	16.1 ± 10.3

density of about 1.5×10^{-11} g cm^{-3} at an altitude of 100 km and 5.2×10^{-13} g cm^{-3} at 300 km.

The profiles of Fig. 15, with a horizontal logarithmic scale, indicate that the number density increases exponentially as altitude decreases. This behavior is consistent with physical models. With no eddy diffusion and no growth of the particles, in a steady state atmosphere where haze is produced at some high level, it can be shown that the density follows an exponential law characterized by a scale height H_{haze}. We note also that the observed slope is not constant. There is hint of an inflexion at about 420 km, thus we can define two scale heights to describe the profiles. In Fig. 15, we overplot the exponential fits $n = n_0 e^{-\frac{z}{H1_{\text{haze}}}}$ for z between 77 and 414 km (26 points used) and $n = n_0 e^{-\frac{z}{H2_{\text{haze}}}}$ for z between 429 and 461 km (3 points used). The values of $H1_{\text{haze}}$ and $H2_{\text{haze}}$ are reported in Table 3 for values of N over 1000. For $H1_{\text{haze}}$, the formal 1-σ error bars in this table are quite small. However, the dispersion of the calculated values of $H1_{\text{haze}}$ suggests that the error bar on the scale height $H1_{\text{haze}}$ is about 2 or 3 km. With a value of about 60 km, $H1_{\text{haze}}$ is of the same order as the scale height calculated for the extinction profile.

For $H2_{\text{haze}}$, the errors are significantly larger because only 3 density values are used for the fit and these values have larger error-bar than densities at lower level. This inflexion is thus marginally detected in our data set. However, this change of scale height between 400 and 500 km has been observed in the density profile retrieved from *Cassini*/UVIS observations of a stellar occultation (Liang et al., 2007). This inflexion corresponds to the clear layer between the main haze layer and the detached haze layer above 500 km observed in ISS images (Porco et al., 2005).

5.5. Spectral behavior of the haze

Here we briefly compare our results with others which adopt a more global approach of the haze optical properties, that is the wavelength dependence of its optical depth of the haze. It is classical to model the scattering by small particles as a power law $\tau(\lambda) = \tau_0 \lambda^{-q}$. Assuming a fractal dimension of 2 as in the model presented before, size of particle could be retrieved from the value of q. At each altitude, the optical depth observed in the continuum wavelengths is adjusted by a power law depending on the two free parameters τ_0 and q. In Fig. 16, the wavelength dependence of the optical depth is presented for a selection of altitudes below 470 km. The best-fit model is overplotted to the data. We observe a change with altitude in the value of the exponent q. The variation of q with altitude is presented in Fig. 17, with its 1-σ error bar. This variation must be considered carefully as the optical depth is very small at high altitude (above 400 km) and very large under 100 km. However, at intermediate altitudes, between 120 and 300 km, we have value of q between 1.7 and 2.2. The observations in 2003 of two ground-based stellar occultation by Titan led to a value of $q = 1.8 \pm 0.5$ at about 250 km and between 0.9 and 2.2 μm (Fig. 17 and Sicardy et al., 2006). Our result is consistent with this value. From DISR measurements, Tomasko et al. (2008) inferred a value of $q = 2.34$ above 84 km, also consistent with our own values.

6. Conclusions

In this paper, we have presented different analysis for the observations of a solar occultation by VIMS. We have shown that molecular species such as CH_4 and CO are detected as they absorb the sunlight along its path in Titan's atmosphere. These absorptions have been modeled and we have underlined some difficulties in measuring precisely the abundances of the detected species. However, we add a new measurement of the CO abundance of 33 ± 10 ppm between 70 and 130 km. This measurement, associated to the other published values will contribute to the study of this species in Titan's atmosphere.

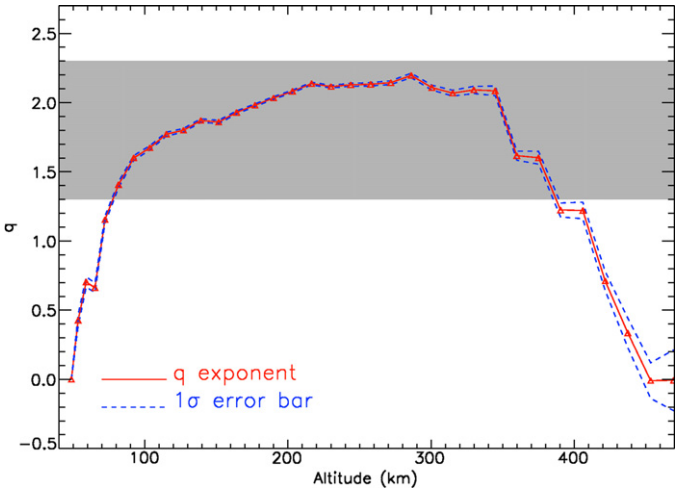

Fig. 17. q values that best fit the optical depth dependence with λ is potted against altitude (solid line) with its 1-σ error bar (dashed line). The gray area represents the interval of values from the 2003 observation of a Titan stellar occultation (Sicardy et al., 2006).

A major result of this paper is the detection of a specific absorption band of aerosols at 3.4 µm. This feature is the signature of C–H vibrations of aliphatic chains on large organic molecules. An observation of a similar feature in the atmosphere of Saturn is an interesting aspect that should be studied further. The observation of this 3.4 µm feature with an increase spectral resolution will help in a better determination of the nature of the aerosol particles responsible for it.

The comparison of the transmission spectra of fractal aerosols with Khare et al.'s tholins optical properties with the observed transmission revealed important chemical differences between actual haze particles and tholins. The N–H and C≡N absorption bands of tholins do not appear in our data.

The aerosol vertical distribution is the third point discussed in this paper using the continuum wavelengths of the observations. We have shown that large numbers, namely over 1000, of spheres par fractal aggregates are needed to fit the observations. The vertical distributions under 500 km follow an exponential law with a scale height of about 60 km. A hint of inflexion at about 420 km is attributed to the clear zone between the main haze layer and the detached haze layer.

Other observations of stellar and solar observation by Titan at different latitudes will reinforce the conclusions of this paper and may reveal latitudinal variations.

Acknowledgments

We thank the Centre National d'Etudes Spatiales (CNES) for supporting the VIMS data interpretation. We also thank B. Bezard and E. Lellouch for their help in the validation of the radiative transfer code and for the data interpretation.

References

Baines, K.H., Drossart, P., Momary, T.W., Formisano, V., Griffith, C., Bellucci, G., Bibring, J.P., Brown, R.H., Buratti, B.J., Capaccioni, F., Cerroni, P., Clark, R.N., Coradini, A., Combes, M., Cruikshank, D.P., Jaumann, R., Langevin, Y., Matson, D.L., McCord, T.B., Mennella, V., Nelson, R.M., Nicholson, P.D., Sicardy, B., Sotin, C., 2005. The atmospheres of Saturn and Titan in the near-infrared: First results of Cassini/VIMS. Earth Moon Planets 96, 119–147.

Baines, K.H., Drossart, P., Lopez-Valverde, M.A., Atreya, S.K., Sotin, C., Momary, T.W., Brown, R.H., Buratti, B.J., Clark, R.N., Nicholson, P.D., 2006. On the discovery of CO nighttime emissions on Titan by Cassini/VIMS: Derived stratospheric abundances and geological implications. Planet. Space Sci. 54, 1552–1562.

Bar-Nun, A., Dimitrov, V., Tomasko, M., 2008. Titan's aerosols: Comparison between our model and DISR findings. Planet. Space Sci. 56, 708–714.

Botet, R., Rannou, P., Cabane, M., 1997. Mean-field approximation of Mie scattering by fractal aggregates of identical spheres. Appl. Opt. 36, 8791–8797.

Boudon, V., Champion, J.P., Gabard, T., Loëte, M., Michelot, F., Pierre, G., Rotger, M., Wenger, C., Rey, M., 2004. Symmetry-adapted tensorial formalism to model rovibrational and rovibronic spectra of molecules pertaining to various point groups. J. Mol. Spectrosc. 228, 620–634.

Brown, R.H., Baines, K.H., Bellucci, G., Bibring, J.P., Buratti, B.J., Capaccioni, F., Cerroni, P., Clark, R.N., Coradini, A., Cruikshank, D.P., Drossart, P., Formisano, V., Jaumann, R., Langevin, Y., Matson, D.L., McCord, T.B., Mennella, V., Miller, E., Nelson, R.M., Nicholson, P.D., Sicardy, B., Sotin, C., 2004. The Cassini Visual and Infrared Mapping Spectrometer (VIMS) Investigation. Space Sci. Rev. 115, 111–168.

Coustenis, A., Achterberg, R.K., Conrath, B.J., Jennings, D.E., Marten, A., Gautier, D., Nixon, C.A., Flasar, F.M., Teanby, N.A., Bézard, B., Samuelson, R.E., Carlson, R.C., Lellouch, E., Bjoraker, G.L., Romani, P.N., Taylor, F.W., Irwin, P.G.J., Fouchet, T., Hubert, A., Orton, G.S., Kunde, V.G., Vinatier, S., Mondellini, J., Abbas, M.M., Courtin, R., 2007. The composition of Titan's stratosphere from Cassini/CIRS mid-infrared spectra. Icarus 189, 35–62.

de Kok, R., Irwin, P.G.J., Teanby, N.A., Lellouch, E., Bézard, B., Vinatier, S., Nixon, C.A., Fletcher, L., Howett, C., Calcutt, S.B., Bowles, N.E., Flasar, F.M., Taylor, F.W., 2007. Oxygen compounds in Titan's stratosphere as observed by Cassini CIRS. Icarus 186, 354–363.

D'Hendecourt, L.B., Allamandola, L.J., 1986. Time dependent chemistry in dense molecular clouds. III. Infrared band cross sections of molecules in the solid state at 10 K. Astron. Astrophys. Ser. 64, 453–467.

Flasar, F.M., Achterberg, R.K., Conrath, B.J., Gierasch, P.J., Kunde, V.G., Nixon, C.A., Bjoraker, G.L., Jennings, D.E., Romani, P.N., Simon-Miller, A.A., Bézard, B., Coustenis, A., Irwin, P.G.J., Teanby, N.A., Brasunas, J., Pearl, J.C., Segura, M.E., Carlson, R.C., Mamoutkine, A., Schinder, P.J., Barucci, A., Courtin, R., Fouchet, T., Gautier, D., Lellouch, E., Marten, A., Prangé, R., Vinatier, S., Strobel, D.F., Calcutt, S.B., Read, P.L., Taylor, F.W., Bowles, N., Samuelson, R.E., Orton, G.S., Spilker, L.J., Owen, T.C., Spencer, J.R., Showalter, M.R., Ferrari, C., Abbas, M.M., Raulin, F., Edgington, S., Ade, P., Wishnow, E.H., 2005. Titan's atmospheric temperatures, winds, and composition. Science 308, 975–978.

Fulchignoni, M., Ferri, F., Angrilli, F., Ball, A.J., Bar-Nun, A., Barucci, M.A., Bettanini, C., Bianchini, G., Borucki, W., Colombatti, G., Coradini, M., Coustenis, A., Debei, S., Falkner, P., Fanti, G., Flamini, E., Gaborit, V., Grard, R., Hamelin, M., Harri, A.M., Hathi, B., Jernej, I., Leese, M.R., Lehto, A., Lion Stoppato, P.F., López-Moreno, J.J., Mäkinen, T., McDonnell, J.A.M., McKay, C.P., Molina-Cuberos, G., Neubauer, F.M., Pirronello, V., Rodrigo, R., Saggin, B., Schwingenschuh, K., Seiff, A., Simões, F., Svedhem, H., Tokano, T., Towner, M.C., Trautner, R., Withers, P., Zarnecki, J.C., 2005. In situ measurements of the physical characteristics of Titan's environment. Nature 438, 785–791.

Griffith, C.A., Penteado, P., Rannou, P., Brown, R., Boudon, V., Baines, K.H., Clark, R., Drossart, P., Buratti, B., Nicholson, P., McKay, C.P., Coustenis, A., Negrao, A., Jaumann, R., 2006. Evidence for a polar ethane cloud on Titan. Science 313, 1620–1622.

Gurwell, M.A., 2004. Submillimeter observations of Titan: Global measures of stratospheric temperature, CO, HCN, HC_3N, and the isotopic ratios $^{12}C/^{13}C$ and $^{14}N/^{15}N$. Astrophys. J. 616, L7–L10.

Gurwell, M.A., Muhleman, D.O., 1995. CO on Titan: Evidence for a well-mixed vertical profile. Icarus 117, 375–382.

Gurwell, M.A., Muhleman, D.O., 2000. CO on Titan: More evidence for a well-mixed vertical profile. Icarus 145, 653–656.

Hidayat, T., Marten, A., Bezard, B., Gautier, D., Owen, T., Matthews, H.E., Paubert, G., 1998. Millimeter and submillimeter heterodyne observations of Titan: The vertical profile of carbon monoxide in its stratosphere. Icarus 133, 109–133.

Imanaka, H., Khare, B.N., Elsila, J.E., Bakes, E.L.O., McKay, C.P., Cruikshank, D.P., Sugita, S., Matsui, T., Zare, R.N., 2004. Laboratory experiments of Titan tholin formed in cold plasma at various pressures: Implications for nitrogen-containing polycyclic aromatic compounds in Titan haze. Icarus 168, 344–366.

Jacovi, R., Bar-Nun, A., 2008. Removal of Titan's noble gases by their trapping in its haze. Icarus 196, 302–304.

Jacquinet-Husson, N., Scott, N.A., Chédin, A., Garceran, K., Armante, R., Chursin, A.A., Barbe, A., Birk, M., Brown, L.R., Camy-Peyret, C., Claveau, C., Clerbaux, C., Coheur, P.F., Dana, V., Daumont, L., Debacker-Barilly, M.R., Flaud, J.M., Goldman, A., Hamdouni, A., Hess, M., Jacquemart, D., Köpke, P., Mandin, J.Y., Massie, S., Mikhailenko, S., Nemtchinov, V., Nikitin, A., Newnham, D., Perrin, A., Perevalov, V.I., Régalia-Jarlot, L., Rublev, A., Schreier, F., Schult, I., Smith, K.M., Tashkun, S.A., Teffo, J.L., Toth, R.A., Tyuterev, V.G., Vander Auwera, J., Varanasi, P., Wagner, G., 2005. The 2003 edition of the GEISA/IASI spectroscopic database. J. Quant. Spectrosc. Radiat. Trans. 95, 429–467.

Jacquinet-Husson, N., Scott, N.A., Chédin, A., Crépeau, L., Armante, R., Capelle, V., Orphal, J., Coustenis, A., Boonne, C., Poulet-Crovisier, N., Barbe, A., Birk, M., Brown, L.R., Camy-Peyret, C., Claveau, C., Chance, K., Christidis, N., Clerbaux, C., Coheur, P.F., Dana, V., Daumont, L., De Backer-Barilly, M.R., Di Lonardo, G., Flaud, J.M., Goldman, A., Hamdouni, A., Hess, M., Hurley, M.D., Jacquemart, D., Kleiner, I., Köpke, P., Mandin, J.Y., Massie, S., Mikhailenko, S., Nemtchinov, V., Nikitin, A., Newnham, D., Perrin, A., Perevalov, V.I., Pinnock, S., Régalia-Jarlot, L., Rinsland, C.P., Rublev, A., Schreier, F., Schult, L., Smith, K.M., Tashkun, S.A., Teffo, J.L., Toth, R.A., Tyuterev, V.G., Vander Auwera, J., Varanasi, P., Wagner, G., 2008. The GEISA

spectroscopic database: Current and future archive for Earth and planetary atmosphere studies. J. Quant. Spectrosc. Radiat. Trans. 109, 1043–1059.

Khare, B.N., Sagan, C., Arakawa, E.T., Suits, F., Callcott, T.A., Williams, M.W., 1984. Optical constants of organic tholins produced in a simulated Titanian atmosphere—From soft X-ray to microwave frequencies. Icarus 60, 127–137.

Lara, L.M., Lellouch, E., López-Moreno, J.J., Rodrigo, R., 1996. Vertical distribution of Titan's atmospheric neutral constituents. J. Geophys. Res. 101, 23261–23283. Erratum: J. Geophys. Res. 103 (1996) 25775.

Lellouch, E., Coustenis, A., Sebag, B., Cuby, J.G., López-Valverde, M., Schmitt, B., Fouchet, T., Crovisier, J., 2003. Titan's 5-μm window: Observations with the Very Large Telescope. Icarus 162, 125–142.

Liang, M.C., Yung, Y.L., Shemansky, D.E., 2007. Photolytically generated aerosols in the mesosphere and thermosphere of Titan. Astrophys. J. 661, L199–L202.

López-Valverde, M.A., Lellouch, E., Coustenis, A., 2005. Carbon monoxide fluorescence from Titan's atmosphere. Icarus 175, 503–521.

Lutz, B.L., de Bergh, C., Owen, T., 1983. Titan—Discovery of carbon monoxide in its atmosphere. Science 220, 1374–1375.

McCord, T.B., Coradini, A., Hibbitts, C.A., Capaccioni, F., Hansen, G.B., Filacchione, G., Clark, R.N., Cerroni, P., Brown, R.H., Baines, K.H., Bellucci, G., Bibring, J.P., Buratti, B.J., Bussoletti, E., Combes, M., Cruikshank, D.P., Drossart, P., Formisano, V., Jaumann, R., Langevin, Y., Matson, D.L., Nelson, R.M., Nicholson, P.D., Sicardy, B., Sotin, C., 2004. Cassini VIMS observations of the Galilean satellites including the VIMS calibration procedure. Icarus 172, 104–126.

Nicholson, P.D., Hedman, M.M., Gierasch, P.J., the Cassini VIMS Team, 2006. Probing Saturn's atmosphere with Procyon. Bull. Am. Astron. Soc. 38, 555.

Niemann, H.B., Atreya, S.K., Bauer, S.J., Carignan, G.R., Demick, J.E., Frost, R.L., Gautier, D., Haberman, J.A., Harpold, D.N., Hunten, D.M., Israel, G., Lunine, J.I., Kasprzak, W.T., Owen, T.C., Paulkovich, M., Raulin, F., Raaen, E., Way, S.H., 2005. The abundances of constituents of Titan's atmosphere from the GCMS instrument on the Huygens probe. Nature 438, 779–784.

Pendleton, Y.J., 1999. Organics in the ISM: Where do they come from? In: D'Hendecourt, L., Joblin, C., Jones, A. (Eds.), Solid Interstellar Matter: The ISO Revolution. EDP Science, Springer-Verlag, Berlin, Paris, pp. 119–134.

Pendleton, Y.J., Allamandola, L.J., 2002. The organic refractory material in the diffuse interstellar medium: Mid-infrared spectroscopic constraints. Astrophys. J. Suppl. Ser. 138, 75–98.

Porco, C.C., Baker, E., Barbara, J., Beurle, K., Brahic, A., Burns, J.A., Charnoz, S., Cooper, N., Dawson, D.D., Del Genio, A.D., Denk, T., Dones, L., Dyudina, U., Evans, M.W., Fussner, S., Giese, B., Grazier, K., Helfenstein, P., Ingersoll, A.P., Jacobson, R.A., Johnson, T.V., McEwen, A., Murray, C.D., Neukum, G., Owen, W.M., Perry, J., Roatsch, T., Spitale, J., Squyres, S., Thomas, P., Tiscareno, M., Turtle, E.P., Vasavada, A.R., Veverka, J., Wagner, R., West, R., 2005. Imaging of Titan from the Cassini spacecraft. Nature 434, 159–168.

Rannou, P., Cabane, M., Botet, R., Chassefière, E., 1997. A new interpretation of scattered light measurements at Titan's limb. J. Geophys. Res. 102, 10997–11014.

Sandford, S.A., Allamandola, L.J., Tielens, A.G.G.M., Sellgren, K., Tapia, M., Pendleton, Y., 1991. The interstellar C–H stretching band near 3.4 microns—Constraints on the composition of organic material in the diffuse interstellar medium. Astrophys. J. 371, 607–620.

Sicardy, B., Colas, F., Widemann, T., Bellucci, A., Beisker, W., Kretlow, M., Ferri, F., Lacour, S., Lecacheux, J., Lellouch, E., Pau, S., Renner, S., Roques, F., Fienga, A., Etienne, C., Martinez, C., Glass, I.S., Baba, D., Nagayama, T., Nagata, T., Itting-Enke, S., Bath, K.L., Bode, H.J., Bode, F., Lüdemann, H., Lüdemann, J., Neubauer, D., Tegtmeier, A., Tegtmeier, C., Thomé, B., Hund, F., deWitt, C., Fraser, B., Jansen, A., Jones, T., Schoenau, P., Turk, C., Meintjies, P., Hernandez, M., Fiel, D., Frappa, E., Peyrot, A., Teng, J.P., Vignand, M., Hesler, G., Payet, T., Howell, R.R., Kidger, M., Ortiz, J.L., Naranjo, O., Rosenzweig, P., Rapaport, M., 2006. The two Titan stellar occultations of 14 November 2003. J. Geophys. Res. (Planets) 111, doi:10.1029/2005JE002624. E11S91.

Tomasko, M.G., Doose, L., Engel, S., Dafoe, L.E., West, R., Lemmon, M., Karkoschka, E., See, C., 2008. A model of Titan's aerosols based on measurements made inside the atmosphere. Planet. Space Sci. 56, 669–707.

Tran, B.N., Ferris, J.P., Chera, J.J., 2003a. The photochemical formation of a titan haze analog. Structural analysis by X-ray photoelectron and infrared spectroscopy. Icarus 162, 114–124.

Tran, B.N., Joseph, J.C., Ferris, J.P., Persans, P.D., Chera, J.J., 2003b. Simulation of Titan haze formation using a photochemical flow reactor: The optical constants of the polymer. Icarus 165, 379–390.

West, R.A., Smith, P.H., 1991. Evidence for aggregate particles in the atmospheres of Titan and Jupiter. Icarus 90, 330–333.

Wong, A.S., Morgan, C.G., Yung, Y.L., Owen, T., 2002. Evolution of CO on Titan. Icarus 155, 382–392.

Yelle, R.V., 1991. Non-LTE models of Titan's upper atmosphere. Astrophys. J. 383, 380–400.